NASA Technical Paper 3462

Experimental Validation of an Integrated Controls-Structures Design Methodology for a Class of Flexible Space Structures

Peiman G. Maghami, Sandeep Gupta, Kenny B. Elliott, Suresh M. Joshi, and Joseph E. Walz

November 1994

NASA Technical Paper 3462

Experimental Validation of an Integrated Controls-Structures Design Methodology for a Class of Flexible Space Structures

Peiman G. Maghami
Langley Research Center • Hampton, Virginia

Sandeep Gupta
ViGYAN, Inc. • Hampton, Virginia

Kenny B. Elliott, Suresh M. Joshi, and Joseph E. Walz
Langley Research Center • Hampton, Virginia

National Aeronautics and Space Administration
Langley Research Center • Hampton, Virginia 23681-0001

November 1994

The use of trademarks or names of manufacturers in this report is for accurate reporting and does not constitute an official endorsement, either expressed or implied, of such products or manufacturers by the National Aeronautics and Space Administration.

This publication is available from the following sources:

NASA Center for AeroSpace Information
800 Elkridge Landing Road
Linthicum Heights, MD 21090-2934
(301) 621-0390

National Technical Information Service (NTIS)
5285 Port Royal Road
Springfield, VA 22161-2171
(703) 487-4650

Nomenclature

$\mathbf{A}$	open-loop plant state matrix
$\overline{\mathbf{A}}$	closed-loop system state matrix
$\mathbf{A}_c$	compensator state matrix
$\mathbf{B}$	control influence matrix for first-order model
$\widetilde{\mathbf{B}}$	control influence matrix for second-order model
$\mathbf{B}_c$	input influence matrix for compensator
$\mathbf{C}_{\text{per}}$	performance output influence matrix for first-order model
$\widetilde{\mathbf{C}}_{\text{per}}$	performance output influence matrix for second-order model
$\overline{\mathbf{C}}_{\text{per}}$	performance output influence matrix for closed-loop system
$\mathbf{C}_r$	rate output influence matrix for first-order model
$\widetilde{\mathbf{C}}_r$	rate output influence matrix for second-order model
$\overline{\mathbf{C}}_u$	control input matrix for closed-loop system
$\mathbf{D}$	damping matrix in second-order model
$\mathbf{D}_r$	damping matrix for reduced second-order model
$\mathcal{E}$	expectation operator
$\mathbf{G}$	output matrix for compensator
$\mathbf{G}_p$	positive semidefinite position gain matrix
$\mathbf{G}_r$	positive semidefinite rate gain matrix
$\mathbf{H}$	disturbance influence matrix for first-order model
$\widetilde{\mathbf{H}}$	disturbance influence matrix for second-order model
$\overline{\mathbf{H}}$	disturbance influence matrix for closed-loop system
$\mathbf{I}_{r \times r}$	$r \times r$ identity matrix
J	objective function for design optimization
$\mathbf{K}$	stiffness matrix in second-order model
$\mathbf{K}_r$	stiffness matrix for reduced second-order model
$\mathbf{M}$	mass matrix in second-order model
M_{max}	maximum allowable mass of system
$\mathbf{M}_r$	mass matrix for reduced second-order model
M_{str}	total mass of structure
m	number of sensors or actuators
$\mathbf{P}$	positive definite solution matrix for positive realness lemma conditions
$\mathbf{P}_c, \mathbf{P}_f$	positive definite solution of Riccati equations
$\text{pow}(k)$	computed power in control signal at time step k
$\mathbf{Q}$, $\mathbf{R}$	weighting matrices for LQG design

$\overline{\mathbf{Q}}$	weighting matrix in positive realness lemma conditions
$\mathbf{Q}_1$	arbitrary positive definite matrix in dissipative LQG design
$\overline{q}_j$	diagonal elements of matrix $\overline{\mathbf{Q}}$
$\mathbf{q}_r$	$r \times 1$ modal coordinates vector
$\mathrm{rms}(k)$	computed root mean square of line-of-sight pointing error at time step k
Tr	matrix trace
$\mathbf{u}$	$m \times 1$ control input vector
$\mathbf{V}$, $\mathbf{W}$	noise covariance matrices, treated as parameters in LQG design
$\mathbf{v}_m$	measurement noise vector
$\mathbf{v}_p$	process noise vector
$\mathbf{w}$	$p \times 1$ disturbance input vector
$\mathbf{x}, \dot{\mathbf{x}}, \ddot{\mathbf{x}}$	$n \times 1$ displacement, velocity, and acceleration vectors, respectively
$\overline{\mathbf{x}}$	state vector of closed-loop system
$y_{\mathrm{per}}^{\max}$	maximum allowable line-of-sight pointing error
$\mathbf{y}_{\mathrm{per}}$	performance output vector
$\mathbf{y}_r$	rate output vector
$\mathbf{z}$	$2n \times 1$ state vector for first-order model
α_i, β_i	controller design parameters for dynamic dissipative controllers
ζ_i	damping ratio for ith mode
$\mathbf{\Gamma}_c$	control influence matrix in modal coordinates, $\mathbf{\Gamma}_c^T = \mathbf{\Phi}^T \widetilde{\mathbf{B}}$
$\mathbf{\Gamma}_d$	disturbance influence matrix in modal coordinates, $\mathbf{\Gamma}_d^T = \mathbf{\Phi}^T \widetilde{\mathbf{H}}$
$\mathbf{\Sigma}_{\overline{\mathbf{x}}}$	state covariance matrix for closed-loop system
$\mathbf{\Phi}$	$n \times r$ matrix with columns that are r structural eigenvectors or mode shapes
ω_i	natural frequency for ith mode

Abbreviations:

ADS	Automated Design Synthesis
CEM	CSI Evolutionary Model
CSI	controls-structures interaction
LOS	line of sight
LQG	linear-quadratic Gaussian
rms	root mean square

Abstract

This paper describes the first experimental validation of an optimization-based integrated controls-structures design methodology for a class of flexible space structures. The Controls-Structures-Interaction (CSI) Evolutionary Model, a laboratory testbed at Langley, is redesigned based on the integrated design methodology with two different dissipative control strategies. The redesigned structure is fabricated, assembled in the laboratory, and experimentally compared with the original test structure. Design guides are proposed and used in the integrated design process to ensure that the resulting structure can be fabricated. Experimental results indicate that the integrated design requires >60 percent less average control power (by thruster actuators) than the conventional control-optimized design while maintaining the required line-of-sight performance, thereby confirming the analytical findings about the superiority of the integrated design methodology. Amenability of the integrated design structure to other control strategies is considered and evaluated analytically and experimentally. This work also demonstrates the capabilities of the Langley-developed design tool CSI-DESIGN, which provides a unified environment for structural and control design.

Introduction

Currently, spacecraft are designed in iterative and separate stages within the structural and control disciplines. The structural design takes into account loading considerations during launch, reboost, or component operational maneuvers. The sizes and masses of mission-related components are estimated and a configuration is developed that maintains the desired component relationships during operations. Next, a control system is designed to orient, guide, and move the spacecraft according to the required performance. Measures for spacecraft performance may take different forms and will depend on requirements to account for pointing jitter, transient response, or power constraints. The control design must also be robust and provide satisfactory closed-loop stability. This compartmentalized approach has been successful in most past missions and works well when a structure with relatively high stiffness is acceptable when nonstructural components are concentrated masses and inertias, or when performance requirements are not stringent. In these cases, the structural modes are beyond the controlled bandwidth, so that minimal control-structure interaction is expected. However, this approach will not meet the stringent performance requirements of future space structures. Several future space missions will utilize large flexible structures in low-Earth and geostationary orbits. Example missions include space science platforms, space processing facilities, and Earth observation systems. Such missions typically will require large distributed-mass components such as booms, solar arrays, and antennas with dimensions that may range from a few meters to hundreds of meters. To minimize the costs of construction, launch, and operations, the structure must be as light as possible. However, the combination of large size and low structural mass leads to increased flexibility and makes more difficult the control of the structure and its components to a specified precise attitude and shape.

Controls-structures interaction (CSI) in the form of destabilizing spillover (refs. 1 and 2) has been verified in simple Earth-based laboratory experiments as well as in the design, analysis, ground development, test, and flight operation of space systems in industry. (See ref. 1.) The current approach to solving CSI problems is to design the spacecraft to avoid undesired dynamic interactions. This effort generally requires either stiffening the structure or slowing the control system response. Stiffening the structure simplifies the control design problem in that the predominant dynamics tend toward a rigid body; but that approach is costly in terms of mass, launch packaging, and fuel consumption. Slowing the control response produces control inputs with less chance of producing destabilizing effects; but a slower response is costly in terms of reduced performance. Neither approach is completely satisfactory. A new design approach is needed that avoids the damaging aspects of controls-structures interaction, while it identifies and exploits the beneficial aspects.

Efforts of the Controls-Structures-Interaction (CSI) program at Langley Research Center (ref. 3)

in developing and experimentally verifying an integrated controls-structures design methodology are described in this paper.

The design methodology is based on the high degree of coupling between the control and structural disciplines in the development of flexible space structures. For example, controllers designed to be robust for unanticipated dynamics may require very low gains and, therefore, may result in conservative designs that do not enhance performance. (See ref. 2.) A structural redesign for high performance would require stiffer and more massive structural elements and increase the frequencies of the higher modes; the resulting control system would require more energy and, therefore, would increase fuel consumption for normal operations.

In the methodology developed here, this coupling is emphasized to integrate structural and control aspects of the design process. Rather than performing structural and control designs in a sequential manner, a unified environment for integrated controls-structures modeling, analysis, and synthesis is developed. Within this environment, a design iteration consists of updating all critical (control and structure) design variables in a single integrated computational framework. An optimization-based procedure with mathematical programming is used for the synthesis of an optimal integrated structure. Many papers that describe optimization-based integrated designs have been published in the last decade. (See ref. 4.) However, most of the techniques in the literature were applied to simple analytical models or laboratory apparatuses. Only recently have studies integrated the design of large flexible space structures, particularly those with thousands of degrees of freedom. (See refs. 5–7.) Further, since the integrated design described herein was fabricated and experimentally tested, a number of realistic constraints have been imposed on the design process, constraints which are not found in other studies. For example, strut designs were chosen to accommodate manufacturing constraints through the use of design curves that relate effective areas and densities.

This paper describes the first experimental verification of the controls-structures integrated design methodology. The phase-0 CSI Evolutionary Model (CEM), a laboratory structure at Langley (shown in fig. 1), was used for this experimental validation. Recently developed dissipative control strategies were considered; these include static dissipative, dynamic dissipative, and dissipative linear-quadratic Gaussian (LQG) controllers because they guarantee closed-loop stability when unmodeled dynamics and parametric uncertainties are present. (See ref. 2.) The performance measure for that verification was the average control energy required to maintain specific line-of-sight (LOS) pointing performance during persistent, band-limited white noise disturbances. An integrated design of the phase-0 CEM was performed to improve the performance of the overall system. Based on these designs, an optimal structure was fabricated and assembled in the laboratory, referred to as the phase-1 CEM. Concurrently, optimal dissipative controllers (control-optimized) were designed for the nominal phase-0 CEM. Active control experiments based on optimal designs of the dissipative controllers for each structure were performed on phase-0 and phase-1 CEM structures to evaluate steady-state disturbance rejection capability of each design. In all cases, the integrated design structure (phase-1 CEM) required substantially less average control power (a reduction by 60 percent or more) than the nominal or conventional structure (phase-0 CEM), while providing slightly better LOS pointing performance. These results clearly demonstrate the advantage of the integrated controls-structures design methodology over the traditional sequential approach and represent the first experimental validation of the integrated design methodology for flexible structures.

The next section describes the mathematical models used for structural dynamics and the dissipative control laws used in this effort. After that discussion is the integrated design procedure for the development of the phase-1 CEM. Then we present an evaluation of the integrated design structure with an alternate control design strategy, the experimental comparisons, and the concluding remarks.

Mathematical Models

Structural Model

The linear, time-invariant, mathematical model of a flexible space structure is given by

$$\mathbf{M}\ddot{\mathbf{x}} + \mathbf{D}\dot{\mathbf{x}} + \mathbf{K}\mathbf{x} = \widetilde{\mathbf{B}}\mathbf{u} + \widetilde{\mathbf{H}}\mathbf{w} \tag{1}$$

where $\mathbf{x}$ is an $n \times 1$ displacement vector, $\mathbf{M}$ is the positive-definite mass matrix, $\mathbf{D}$ is the positive semidefinite open-loop damping matrix, $\mathbf{K}$ is the positive semidefinite stiffness matrix, $\widetilde{\mathbf{B}}$ is an $n \times m$ control influence matrix, $\widetilde{\mathbf{H}}$ is an $n \times p$ disturbance influence matrix, $\mathbf{u}$ is the $m \times 1$ control input vector, and $\mathbf{w}$ is the $p \times 1$ disturbance vector. The output equations are

$$\left.\begin{aligned} \mathbf{y}_r &= \widetilde{\mathbf{C}}_r\dot{\mathbf{x}} \\ \mathbf{y}_{\text{per}} &= \widetilde{\mathbf{C}}_{\text{per}}\mathbf{x} \end{aligned}\right\} \tag{2}$$

where $\mathbf{y}_r$ is the rate measurement output vector and $\mathbf{y}_{\text{per}}$ is a performance output vector. The matrices $\widetilde{\mathbf{C}}_r$ and $\widetilde{\mathbf{C}}_{\text{per}}$ are the corresponding output influence matrices. The second-order representation of the structure given in equation (1) is obtained by finite element modeling of the structure. The order of a flexible space structure can be quite large. For design and analysis purposes, the order of the system is reduced to a design size by a modal truncation approach wherein every significant mode in the input-output characterization of the plant is retained and the remaining modes are truncated; or the order of the system is reduced by some other mode selection approach. The system equations in modal coordinates for the retained modes are written as

$$\begin{aligned}\mathbf{M}_r\ddot{\mathbf{q}}_r + \mathbf{D}_r\dot{\mathbf{q}}_r + \mathbf{K}_r\mathbf{q}_r &= \mathbf{\Phi}^T\widetilde{\mathbf{B}}\mathbf{u} + \mathbf{\Phi}^T\widetilde{\mathbf{H}}\mathbf{w} \\ &\equiv \mathbf{\Gamma}_c^T\mathbf{u} + \mathbf{\Gamma}_d^T\mathbf{w} \qquad (3)\end{aligned}$$

where $\mathbf{q}_r$ is an $r \times 1$ vector of modal amplitudes; $\mathbf{M}_r$, $\mathbf{D}_r$, and $\mathbf{K}_r$ are, respectively, the generalized mass, damping, and stiffness matrices; and $\mathbf{\Phi}$ is an $n \times r$ matrix the columns of which are the r structural eigenvectors associated with the included modes. If the mode shapes are normalized with respect to the mass matrix and modal damping is assumed, then $\mathbf{M}_r = \mathbf{I}_{r\times r}$, $\mathbf{D}_r = \text{Diag}[2\zeta_1\omega_1, \ldots, 2\zeta_r\omega_r]$, and $\mathbf{K}_r = \text{Diag}[\omega_1^2, \ldots, \omega_r^2]$, where ω_i and ζ_i $(i = 1, \ldots, r)$ are the open-loop frequencies and damping ratios. With collocated and compatible measurement sensors and control actuators,

$$\begin{aligned}\mathbf{y}_r &= \widetilde{\mathbf{B}}^T\mathbf{\Phi}\dot{\mathbf{q}}_r \\ &= \mathbf{\Gamma}_c\dot{\mathbf{q}}_r \qquad (4)\end{aligned}$$

Note that the collocation of these sensors and actuators is necessary for the implementation of the dissipative controllers. This collocation guarantees that the system is minimum phase such that all transmission zeros are in the left-half plane and will enhance the stability robustness of the overall system. (See ref. 2.)

After defining the state vector $\mathbf{z} = [\,\mathbf{q}_r \quad \dot{\mathbf{q}}_r\,]^T$, we can write the dynamics of the system into the first-order form

$$\dot{\mathbf{z}} = \mathbf{A}\mathbf{z} + \mathbf{B}\mathbf{u} + \mathbf{H}\mathbf{w} \qquad (5)$$

where

$$\mathbf{A} = \begin{bmatrix} 0 & \mathbf{I}_{r\times r} \\ -\mathbf{K}_r & -\mathbf{D}_r \end{bmatrix}$$

$$\mathbf{B} = \begin{bmatrix} 0 \\ \mathbf{\Gamma}_c^T \end{bmatrix}$$

$$\mathbf{H} = \begin{bmatrix} 0 \\ \mathbf{\Gamma}_d^T \end{bmatrix}$$

Actuator and sensor dynamics are assumed negligible. The rate measurement and performance output vectors are given by

$$\begin{aligned}\mathbf{y}_r &= [\,0 \quad \mathbf{\Gamma}_c\,]\mathbf{z} \\ &\equiv \mathbf{C}_r\mathbf{z} \\ \mathbf{y}_{\text{per}} &= [\,\widetilde{\mathbf{C}}_{\text{per}}\mathbf{\Phi} \quad 0\,]\mathbf{z} \\ &\equiv \mathbf{C}_{\text{per}}\mathbf{z}\end{aligned}$$

Here, $\mathbf{C}_{\text{per}}$ is the output influence matrix associated with $\mathbf{y}_{\text{per}}$. For example, in this work, the performance vector $\mathbf{y}_{\text{per}}$ corresponds to the 2×1 LOS pointing error vector and $\mathbf{C}_{\text{per}}$ is the output matrix for the LOS pointing error.

Figure 2 shows the feedback control configuration used to synthesize the integrated controls-structures design and the active control experiments. The persistent disturbance noise $\mathbf{w}(t)$ is applied to the structure at the disturbance locations, and an LOS pointing error vector $\mathbf{y}_{\text{per}}(t)$, measured by a laser detector, must be maintained within desired specifications. The feedback compensator generates control input $\mathbf{u}(t)$ from the measured outputs $\mathbf{y}_r(t)$. The feedback compensators are dissipative controllers described next.

Controller Design Methods

Control system design for flexible space structures is challenging because of the special dynamic characteristics involved. A large number of structural modes within the controller bandwidth; low, closely spaced structural frequencies; very small inherent damping; and insufficient knowledge of the parameters all contribute to the challenge. The controller must be of a reasonably low order to be implementable; it must also satisfy the performance specifications (i.e., constraints on root-mean-square (rms) pointing error and desired closed-loop bandwidth). The controller must also be robust to nonparametric uncertainties (i.e., unmodeled structural modes) and to parametric uncertainties (i.e., errors related to the design model).

Two major categories of controller design methods for flexible space structures are model-based and dissipative controllers. A model-based controller generally consists of a state estimator (a Kalman-Bucy filter or an observer) and a state feedback controller. The state estimator utilizes the knowledge of the design model (the rotational rigid-body modes and a few elastic modes) for prediction. With multivariable frequency-domain design methods, such controllers can be made robust to unmodeled structural dynamics; that is, the spillover effect can be overcome. (See ref. 2.) However, such controllers generally are sensitive to uncertainties in the design model, in particular, to uncertainty in the structural mode frequencies. (See refs. 2 and 8.) An analytical explanation of this instability mechanism is found in reference 8.

Dissipative controllers utilize special passivity input-output properties of the structural model and offer robust stability to both nonparametric and parametric uncertainties. (See refs. 2 and 8.) Therefore, they offer an attractive alternative to model-based controllers.

Static dissipative controller. The simplest system of this type is the static or constant-gain dissipative controller. Using collocated actuators such as torquers with attitude and attitude rate sensors, and thrusters with linear position and linear velocity sensors, we can write the constant-gain dissipative control law as

$$\mathbf{u} = -\mathbf{G}_r\mathbf{y}_r - \mathbf{G}_p\mathbf{y}_p \tag{6}$$

where $\mathbf{y}_r$ and $\mathbf{y}_p$ are $m \times 1$ rate and position measurement vectors (where m is the number of sensors) and $\mathbf{G}_r$ and $\mathbf{G}_p$ are the $m \times m$ symmetric, positive semidefinite rate and position gain matrices, respectively. This control law has been proven to give guaranteed closed-loop stability despite unmodeled elastic modes, parameter errors, and certain types of actuator and sensor nonlinearities (such as saturation and dead zone) as long as actuator dynamics are limited to zero- or first-order forms. (See ref. 2.) For space structures with zero-frequency, rigid-body modes, position feedback is essential to ensure stability of the closed-loop system. However, for the ground-based structure considered in this paper, rate feedback alone is sufficient to guarantee stability for the structures with nonzero-frequency suspension modes. Therefore, only rate feedback is considered. The drawback of this controller is that the achievable performance is inherently limited because of its simple mathematical structure.

Dynamic dissipative controller. To obtain higher performance yet retain the highly desirable robust stability, dynamic dissipative compensators can be used. The main characteristic of all dissipative controllers is that they do not rely on the knowledge of the design model to ensure stability, although they do utilize it to obtain the best possible performance. An n_c-order (two-level) dynamic dissipative controller is given by

$$\dot{\mathbf{x}}_c = \mathbf{A}_c\mathbf{x}_c + \mathbf{B}_c\mathbf{y}_r \tag{7}$$

$$\mathbf{u} = -\mathbf{G}\mathbf{x}_c - \mathbf{G}_r\mathbf{y}_r - \mathbf{G}_p\mathbf{y}_p \tag{8}$$

where $\mathbf{A}_c$, $\mathbf{B}_c$, and $\mathbf{G}$ are the compensator system, input, and output matrices, respectively; and $\mathbf{G}_r$ and $\mathbf{G}_p$ are symmetric, positive semidefinite rate and position gain matrices corresponding to the static dissipative inner loop. For ground test articles with no zero-frequency rigid-body modes, position feedback is not necessary. The dynamic compensator in the outer loop is dissipative if its transfer function is strictly positive real. The positive realness lemma or the Kalman-Yacubovich lemma (ref. 9) assures this condition when $\mathbf{A}_c$ is Hurwitz, $(\mathbf{A}_c, \mathbf{B}_c)$ is controllable, $(\mathbf{A}_c, \mathbf{G})$ is observable, and the following conditions are satisfied:

$$\mathbf{A}_c^T\mathbf{P} + \mathbf{P}\mathbf{A}_c = -\overline{\mathbf{Q}} \tag{9}$$

$$\mathbf{G} = \mathbf{B}_c^T\mathbf{P} \tag{10}$$

where $\mathbf{P} = \mathbf{P}^T > 0$ and the weighting matrix $\overline{\mathbf{Q}} = \overline{\mathbf{Q}}^T \geq 0$. Similar to the static dissipative controller, this control law has been proven to give guaranteed closed-loop stability despite unmodeled elastic modes and parameter errors. (See ref. 8.)

Dissipative LQG optimal controller. Design methods with LQG have been popular in the synthesis of feedback controllers. Although the nominal closed-loop stability, that is, the stability of the nominal system, is guaranteed by LQG theory, stability is by no means guaranteed in the presence of unmodeled dynamics and the parametric uncertainties commonly associated with flexible space structures. However, if the optimal compensator is restricted to be dissipative, then closed-loop stability can be guaranteed. The constraints on the LQG compensator design matrices that lead to a dissipative compensator have been developed in reference 10 and are summarized below.

For the linear time-invariant system

$$\left.\begin{aligned} \dot{\mathbf{x}} &= \mathbf{A}\mathbf{x} + \mathbf{B}\mathbf{u} + \mathbf{v}_p \\ \mathbf{y} &= \mathbf{C}\mathbf{x} + \mathbf{v}_m \end{aligned}\right\} \tag{11}$$

the LQG optimal compensator is given by

$$\left.\begin{aligned}\dot{\hat{\mathbf{x}}} &= (\mathbf{A} - \mathbf{B}\mathbf{R}^{-1}\mathbf{B}^T\mathbf{P}_c - \mathbf{P}_f\mathbf{C}^T\mathbf{V}_m^{-1}\mathbf{C})\hat{\mathbf{x}} + \mathbf{P}_f\mathbf{C}^T\mathbf{V}_m^{-1}\mathbf{y} \\ \mathbf{u} &= -\mathbf{R}^{-1}\mathbf{B}^T\mathbf{P}_c\hat{\mathbf{x}}\end{aligned}\right\} \tag{12}$$

where $\mathbf{P}_c$ and $\mathbf{P}_f$ are solutions of the Riccati equations

$$\left.\begin{aligned}\mathbf{A}^T\mathbf{P}_c + \mathbf{P}_c\mathbf{A} - \mathbf{P}_c\mathbf{B}\mathbf{R}^{-1}\mathbf{B}^T\mathbf{P}_c + \mathbf{Q} = 0 \\ \mathbf{P}_f\mathbf{A}^T + \mathbf{A}\mathbf{P}_f - \mathbf{P}_f\mathbf{C}^T\mathbf{V}_m^{-1}\mathbf{C}\mathbf{P}_f + \mathbf{V}_p = 0\end{aligned}\right\} \tag{13}$$

where $\mathbf{Q} \geq 0$ and $\mathbf{R} > 0$ are the weighting matrices and $\mathbf{V}_m > 0$ and $\mathbf{V}_p \geq 0$ are the noise covariance matrices. The matrices $\mathbf{V}_m$ and $\mathbf{V}_p$ have to satisfy certain constraints, as specified later, for the compensator to be dissipative. If the linear system of equation (11) is passive (i.e., its transfer function is positive real), which is the case for flexible space structures with velocity output, the system matrices satisfy the following conditions of the positive real lemma for some $\mathbf{P} > 0$ and $\hat{\mathbf{Q}} \geq 0$:

$$\left.\begin{aligned}\mathbf{A}^T\mathbf{P} + \mathbf{P}\mathbf{A} &= -\hat{\mathbf{Q}} \\ \mathbf{P}\mathbf{B} &= \mathbf{C}^T\end{aligned}\right\} \tag{14}$$

If $\mathbf{V}_p$ and $\mathbf{V}_m$ are constructed as

$$\left.\begin{aligned}\mathbf{V}_p &= \mathbf{P}^{-1}\hat{\mathbf{Q}}\mathbf{P}^{-1} + \mathbf{B}\mathbf{R}^{-1}\mathbf{B}^T \\ \mathbf{V}_m &= \mathbf{R}\end{aligned}\right\} \tag{15}$$

$\mathbf{R} > 0$ is arbitrary, and $\mathbf{Q}$ is a positive definite matrix that satisfies

$$\mathbf{Q} - \mathbf{P}\mathbf{B}\mathbf{R}^{-1}\mathbf{B}^T\mathbf{P} \equiv \mathbf{Q}_1 > 0 \tag{16}$$

where $\mathbf{Q}_1 > 0$ is arbitrary, then the compensator in equations (12) is dissipative. (See ref. 8.) As before, the dissipative nature of the compensator guarantees closed-loop stability in the presence of unmodeled dynamics and parametric uncertainties.

Integrated Design of CEM

The phase-0 CEM (fig. 1) consists of a 62-bay central truss (each bay is 10 in. long), two vertical towers, and two horizontal booms. The structure is suspended from the ceiling about 840 in. above the main truss by two cables as shown. (See fig. 1.) A laser source is mounted at the top of one tower and a reflector with a mirrored surface is mounted on the other. A laser beam is reflected by the mirrored surface onto a detector surface 660 in. above the reflector. The LOS pointing problem is to maintain the laser at its nominal position on the detector surface. Eight proportional bidirectional gas thrusters with a maximum output force of 4.4 lb each are available at stations 1 to 8 as shown in figure 1. Almost collocated with the thrusters at the eight stations are servo-accelerometers to provide output measurements. Accelerometer signals are subsequently integrated with the aid of washout filters to provide rate information. A more detailed description of the phase-0 CEM is given in reference 11.

The phase-0 CEM is representative of flexible space structures in that a number of low-frequency, closely spaced modes are within the bandwidth of its controllers, the inherent damping is low, and the modal parameters are uncertain. However, it differs from space structures in that it is under the influence of gravity and has no zero-frequency rigid-body modes. The finite element model of the system has 3216 degrees of freedom; therefore, a major computational effort is required to solve the structural eigenvalue problem of that size. The control design model consisted of the first 30 modes of the structure, which include 24 flexible and 6 suspension modes (nonzero-frequency rigid-body modes due to suspension of the structure in gravity). A modal damping ratio of 0.1 percent was assumed. The modal frequencies of the first 10 modes of the nominal phase-0 CEM are presented in table I. The first six modes range from 0.147 to 0.874 Hz and are the suspension modes. Modes 7 and 8 are the first two bending modes (lateral and vertical) and mode 9 is the first torsional mode of the structure.

For the integrated design problem, white-noise disturbances of unit intensity are applied to the structure at stations 1 and 2, and the feedback control inputs are applied at stations 3 through 8. Past experience with the phase-0 CEM structure has shown that actuators at stations 7 and 8 could easily destabilize laser tower modes, in the form of spillover destabilization, which is typically observed in the control of flexible structures. Thus, although actuators 7 and 8 were at the most efficient locations for exciting the structure, they were included for control feedback instead so that we could consider the robust stability issue objectively. After actuators 7 and 8, actuators 1 and 2 were the most effective means by which to excite the structure. Therefore, actuators 1 and 2 were chosen as disturbance sources for integrated design and experimental validation. With no appreciable sensor and actuator dynamics considered, the system equations are given by equation (5),

where the matrix $\mathbf{\Gamma}_c$ contains the modal displacements at the control stations 3 through 8 and the matrix $\mathbf{\Gamma}_d$ contains modal displacements at the disturbance stations 1 and 2. The performance vector $\mathbf{y}_{\text{per}}$ is the LOS pointing error or deviation of the laser point on the detector system from its nominal position in local X and Y coordinates.

The design optimization problem is to minimize the steady-state average control power, maintain specified rms LOS pointing performance in the presence of a persistent white-noise input at the disturbance stations, and sustain the total mass budget of the nominal phase-0 CEM. Mathematically, the design problem is to minimize

$$J = \lim_{t\to\infty}\left(Tr\left\{\mathcal{E}\left[\mathbf{u}(t)\,\mathbf{u}^T(t)\right]\right\}\right) \tag{17}$$

with respect to structural and control design variables, subject to the constraints

$$\lim_{t\to\infty}\left(Tr\left\{\mathcal{E}\left[\mathbf{y}_{\text{per}}(t)\,\mathbf{y}_{\text{per}}^T(t)\right]\right\}\right)^{\frac{1}{2}} \le y_{\text{per}}^{\max} \tag{18}$$

$$M_{\text{str}} \le M_{\max} \tag{19}$$

where J is the objective function for the design optimization, $y_{\text{per}}^{\max}$ is the maximum allowable LOS pointing error, M_{str} is the total mass of the structure and is obtained from the mass matrix of the finite element analysis routine, $M_{\max}$ is the mass budget, Tr denotes the trace of the matrix, and $\mathcal{E}$ is the expectation operator.

In the case of the CEM, rms LOS pointing accuracy was chosen as the performance measure, with $y_{\text{per}}^{\max}$ equal to 2.4 in., approximately a factor-of-10 reduction from the open-loop rms LOS pointing capability for the phase-0 CEM structure (22.54 in.); $M_{\max}$ was chosen to be 1.92 lb-sec^2/in., which was the nominal mass of the phase-0 CEM structure.

Based on any dissipative controllers described earlier, the closed-loop system dynamics can be written as

$$\left.\begin{aligned} \dot{\overline{\mathbf{x}}} &= \overline{\mathbf{A}}\overline{\mathbf{x}} + \overline{\mathbf{H}}\mathbf{w} \\ \mathbf{y}_{\text{per}} &= \overline{\mathbf{C}}_{\text{per}}\overline{\mathbf{x}} \\ \mathbf{u} &= \overline{\mathbf{C}}_u\overline{\mathbf{x}} \end{aligned}\right\} \tag{20}$$

where $\overline{\mathbf{x}}$ is the state vector for the closed-loop dynamics; $\mathbf{w}$ is the zero-mean, white-noise disturbance; $\mathbf{y}_{\text{per}}$ is the LOS pointing performance; $\mathbf{u}$ is the control vector; and $\overline{\mathbf{A}}$, $\overline{\mathbf{H}}$, $\overline{\mathbf{C}}_{\text{per}}$, and $\overline{\mathbf{C}}_u$ are the corresponding system matrices. The steady-state covariance matrix for the closed-loop state $\mathbf{\Sigma}_{\overline{\mathbf{x}}}$ is computed by solving the following Lyapunov (ref. 12) equation:

$$\overline{\mathbf{A}}\mathbf{\Sigma}_{\overline{\mathbf{x}}} + \mathbf{\Sigma}_{\overline{\mathbf{x}}}\overline{\mathbf{A}}^T + \overline{\mathbf{H}}\mathbf{\Sigma}_{\mathbf{w}}\overline{\mathbf{H}}^T = 0 \tag{21}$$

where $\mathbf{\Sigma}_{\mathbf{w}}$ is the covariance matrix for $\mathbf{w}(t)$. The steady-state average control power is given as

$$\lim_{t\to\infty} Tr\left\{\mathcal{E}\left[\mathbf{u}(t)\,\mathbf{u}^T(t)\right]\right\} = Tr\left(\overline{\mathbf{C}}_u\mathbf{\Sigma}_{\overline{\mathbf{x}}}\overline{\mathbf{C}}_u^T\right) \tag{22}$$

and the rms LOS pointing performance is

$$\lim_{t\to\infty}\left(Tr\left\{\mathcal{E}\left[\mathbf{y}_{\text{per}}(t)\,\mathbf{y}_{\text{per}}^T(t)\right]\right\}\right)^{\frac{1}{2}} = \left[Tr\left(\overline{\mathbf{C}}_{\text{per}}\mathbf{\Sigma}_{\overline{\mathbf{x}}}\overline{\mathbf{C}}_{\text{per}}^T\right)\right]^{\frac{1}{2}} \tag{23}$$

A typical strut of the phase-1 CEM design is shown in figure 3. The strut has three sections; the node ball, the tube, and the connection hardware. The effective area of the strut was chosen as the structural design variable for the integrated design. The effective area represents the stiffness of the strut and the portion of the node ball that contributes to the stiffness between the centers of each node.

The strut can be thought of as three springs in series. The end springs represent the stiffness of the node balls and connection hardware; the center spring is the stiffness of the tube. In an ideal design with uniform struts, the effective area would be the cross-sectional area of the strut. However, for the effective area of the struts shown in figure 3, we took into consideration the nonuniformity of the strut and node ball geometry and the losses across the joining surfaces. Associated with each effective area is a minimum effective density corresponding to the lightest strut that can be manufactured for the specified strut stiffness. The effective density, together with the effective area and the lengths between nodes, gives the mass of the strut. The combination of effective area and effective density defines the stiffness and mass properties of the structure. To ensure that the strut could be manufactured, design guides were developed empirically that defined a two-dimensional design space of manufacturable struts. The design space gives the relationship between the effective area and density for a particular strut design. Obviously, the design space is dependent on the type of strut and node ball design chosen.

The strut design considered here was developed to allow a continuously variable effective area. By starting with a stock tube and machining the tube to a specified outer diameter, a variety of effective areas could be manufactured. Therefore, instead of a design space consisting of a family of point designs, the design space could be considered continuous. The

design guide for the longerons and battens is shown in figure 4 and the design guide for the diagonals is shown in figure 5. The shape of the curves on the left side of the figure, corresponding to the lowest effective area, is governed by the load capacity of the tube portion of the strut, whereas the right side, corresponding to the highest effective areas, is governed by manufacturability considerations.

For the structural design, the CEM structure was divided into the seven sections shown in figure 6. Three sections are in the main truss, one section is for the laser tower, one section is for the reflector tower, and one section each is for the two horizontal booms. Three structural design variables were used in each section, namely, effective areas of the longerons, the battens, and the diagonals. Thus, the integrated design of the structure involved 21 structural design variables. The control design variables for static and dynamic dissipative controllers are described in later sections.

The integrated design software tool CSI-DESIGN is being developed at Langley and was used to perform the numerical nonlinear programming optimizations. The CSI-DESIGN tool uses in-core database architecture and public domain software. (See refs. 13–15.) The package has control, structural, and optimization modules linked in a unified environment to perform design iterations on both structural and control design variables. A description of the contents of the CSI-DESIGN structural module may be found in reference 16. A four-processor Alliant FX-80 digital computer was used to perform design optimization with the Automated Design Synthesis (ADS) software. (See ref. 13.) Gradient computations were performed with finite difference approximations. An interior penalty function method of ADS was used to solve the nonlinear programming problems. In this method, the constrained optimization problem is transformed into an unconstrained problem through creation of a pseudo-objective function that is the sum of the original objective function and an imposed penalty function (which is a function of the constraints). (See ref. 17.) The Reverse-Cuthill-McKee algorithm (ref. 18) for minimizing the bandwidth of the banded stiffness and mass matrices was used to reduce computational and memory requirements. Additionally, analytical expressions for eigenvalue and eigenvector sensitivity (with respect to the structural design variables, (ref. 19)) were used in the integrated design process to approximate the eigenvalues and eigenvectors at design points that are in the neighborhood of the nominal design point. This approximation was in the form of a first-order Taylor series approximation and resulted in substantial computational savings because it removed the need for costly computation of structural eigenvalues and eigenvectors at many of the optimization moves.

Static Dissipative Controller

The test article has no zero-frequency rigid-body modes so only rate feedback is employed for the static dissipative controller. Thus,

$$\mathbf{u} = -\mathbf{G}_r \mathbf{y}_r \tag{24}$$

A 6×6 diagonal matrix was chosen for $\mathbf{G}_r$, the elements of which were the six control design variables. A diagonal gain matrix is used for simplicity and because the resulting decentralized controller generally exhibits superior performance robustness. The closed-loop matrices (in eq. (20)) for the static dissipative controller are

$$\left.\begin{aligned} \overline{\mathbf{A}} &= \begin{bmatrix} 0 & \mathbf{I}_{r \times r} \\ -\mathbf{K}_r & -\mathbf{D}_r - \mathbf{\Gamma}_c^T \mathbf{G}_r \mathbf{\Gamma}_c \end{bmatrix} \\ \overline{\mathbf{H}} &= \mathbf{H} \\ \overline{\mathbf{C}}_{\text{per}} &= \mathbf{C}_{\text{per}} \\ \overline{\mathbf{C}}_u &= -[0 \quad \mathbf{G}_r \mathbf{\Gamma}_c] \end{aligned}\right\} \tag{25}$$

The average control power and the rms LOS pointing performance for static dissipative controllers are computed from equations (22) and (23). A total of 27 design variables, 21 structural design variables, and 6 control design variables were used in the integrated design optimization for the static dissipative integrated design.

The results of the design optimizations are summarized in table II. The control-optimized design was performed first (with the structural design variables fixed at the nominal values for the phase-0 CEM) and required an average steady-state control power of 7.11 lb^2 to maintain rms LOS pointing performance at 2.4 in. Next, an integrated design was performed wherein the average control power was minimized with respect to both control and structural design variables. The results (table II) indicate an average control power of 4.21 lb^2 to maintain the same rms LOS pointing performance. The integrated design results in a reduction of more than 40 percent in the average control power over the conventional design for the same rms LOS pointing performance. The effective areas for the structural design are shown in table III. Keeping in mind that the tube cross-sectional areas of the nominal phase-0 CEM are 0.134 in^2 for the longerons and battens and 0.124 in^2 for the

diagonals, it is observed that the longerons for all three sections of the main truss, particularly the section closest to the disturbance sources, and the laser tower are considerably stiffened, whereas the horizontal booms and the reflector tower became more flexible, partially to satisfy the mass constraint. Generally, all the diagonals and the battens decreased in size, mainly because the design optimization had to satisfy a constraint on the total mass (i.e., the mass of the phase-1 CEM design had to be less than or equal to the mass of phase-0 CEM design). Consequently, mass was taken from the battens and diagonals and was redistributed to the longerons of some sections because they are quite effective in increasing the stiffness of a section. This trend may be attributed to a trade-off between structural controllability, observability, and excitability. The areas near the disturbance sources (i.e., stations 1 and 2) were stiffened to reduce the structure sensitivity to external disturbances at those locations and at the same time ensure that no appreciable loss of controllability and/or observability occurred. The control gains for the control-optimized and the integrated designs are shown in table IV. Generally, the gains for the phase-1 CEM design are considerably less than those for the phase-0 CEM design (except for actuator 6). This difference is expected because the required control power for the phase-1 CEM is significantly less than that of the phase-0 CEM.

Dynamic Dissipative Controller

The dynamic dissipative controller represented by equations (7) and (8) with no static inner loop ($\mathbf{G}_p$ and $\mathbf{G}_r = 0$) was used with $\mathbf{A}_c$ (consisting of six second-order blocks) and the compensator influence matrix $\mathbf{B}_c$ as

$$\mathbf{A}_c = \begin{bmatrix} \mathbf{A}_{c1} & 0 & \dots & 0 \\ 0 & \mathbf{A}_{c2} & \dots & 0 \\ \vdots & \vdots & \ddots & \vdots \\ 0 & 0 & \dots & \mathbf{A}_{c6} \end{bmatrix} \tag{26}$$

$$\mathbf{B}_c = \begin{bmatrix} \mathbf{B}_{c1} & 0 & \dots & 0 \\ 0 & \mathbf{B}_{c2} & \dots & 0 \\ \vdots & \vdots & \ddots & \vdots \\ 0 & 0 & \dots & \mathbf{B}_{c6} \end{bmatrix} \tag{27}$$

where $\mathbf{A}_{ci}$ and $\mathbf{B}_{ci}$ $(i = 1,2,\dots,6)$ are, respectively, a 2×2 matrix and a 2×1 vector, defined as

$$\left.\begin{aligned} \mathbf{A}_{ci} &= \begin{bmatrix} 0 & 1 \\ -\alpha_i & -\beta_i \end{bmatrix} \\ \mathbf{B}_{ci} &= \begin{bmatrix} 0 \\ 1 \end{bmatrix} \end{aligned}\right\} \tag{28}$$

Furthermore, $\overline{\mathbf{Q}}$ in equation (9) was assumed to be diagonal. That is,

$$\overline{\mathbf{Q}} = \mathrm{diag}(\overline{q}_1, \overline{q}_2, \dots, \overline{q}_{12}) \tag{29}$$

For the dynamic dissipative controller, the closed-loop system matrices are

$$\left.\begin{aligned} \overline{\mathbf{A}} &= \begin{bmatrix} \mathbf{A} & -\mathbf{B}\mathbf{G} \\ \mathbf{B}_c\mathbf{C}_r & \mathbf{A}_c \end{bmatrix} \\ \overline{\mathbf{H}} &= \begin{bmatrix} \mathbf{H} \\ 0 \end{bmatrix} \\ \overline{\mathbf{C}} &= [\,\mathbf{C}_{\mathrm{per}} \quad 0\,] \end{aligned}\right\} \tag{30}$$

For average control power computation, $\overline{\mathbf{C}}_u = -[0 \quad \mathbf{G}]^T$. Again, equations (22) and (23) are used for computing control power and the rms LOS pointing performance. Here, the scalar variables α_i, β_i, $(i = 1,2,\dots,6)$, and $\overline{q}_j$ $(j = 1,2,\dots,12)$ were chosen for the control design variables. Thus, 24 control design variables are included; with 21 structural design variables, the total number of design variables becomes 45.

Table II shows the results of designs with the dynamic dissipative controller. The control-optimized design for the phase-0 CEM required a control power of 6.41 lb^2 to maintain an rms LOS pointing performance of 2.4 in. The integrated design reduces the average control power by 44 percent more than the conventional design to 3.64 lb^2. The effective areas of the structural elements for integrated design with the dynamic dissipative compensator are in table V. Effective areas for longerons, battens, and diagonals for the integrated design with dynamic dissipative controllers show the same trends as those for the static dissipative controller in table III. Control design variables for the control-optimized design variables and the integrated design are shown in table VI. Figure 7 shows a comparison of the maximum and minimum singular-value plots of optimal dynamic dissipative controllers for the phase-0 CEM (dashed lines) and phase-1 CEM (solid lines). The controller gains are generally smaller throughout the frequency spectrum except in the very low-frequency region. However, the power distribution shapes of the two controllers are somewhat similar.

The results obtained for both the static and dynamic dissipative controllers clearly show that integrated controls-structures design methodology can yield a substantially superior overall design than the conventional sequential design scenario. Moreover, a comparison of tables III and V shows that the optimal structures for both control designs exhibit similar trends. In fact, the structural design variables for the two optimal structures are within 20 percent of each other. Therefore, a structural design close to both was chosen for fabrication and assembly. The structural elements of the optimal structure, the phase-1 CEM, are given in table VII. For comparison, recall that the effective areas of battens and longerons of the phase-0 CEM are 0.134 in^2 and the effective areas for diagonals are 0.124 in^2. Note that the production values of the elements for the assembled structure were chosen to approximate the design trends from the numerical studies; however, to avoid excessive costs, the number of different size struts was kept as small as possible. In consonance with the design trends, all diagonals and battens were chosen of the same size. Four different sizes of the longerons were used for the various sections as shown in table VII. The modal frequencies of the first 10 modes of the fabricated phase-1 CEM are presented in table VIII. These frequencies indicate that the first six frequencies associated with the suspended structure have not been changed significantly, mainly because the changes in the structure can affect these frequencies only through changing the center of mass of the structure and not directly as for the flexible modes. On the other hand, the frequencies of the flexible modes, particularly the second and third flexible modes, have increased considerably (as much as 30 percent). The second flexible mode frequency increased from 1.74 to 2.25 Hz and the third flexible mode frequency from 1.88 to 2.40 Hz, making these modes and the structure less sensitive to disturbances at stations 1 and 2.

Evaluation With Alternate Controller

The integrated design process that produced the phase-1 CEM was performed with static and dynamic dissipative controllers as the control design strategy. In realistic spacecraft design, deciding on a specific control architecture during the preliminary structural design phase may not be feasible. Therefore, an exploration is desirable to ascertain the impact on the overall system performance when an alternate control design strategy is employed with the integrated design structure. Control-optimized dissipative LQG compensators were designed and tested for both the phase-0 CEM and the phase-1 CEM for one such comparison.

From matrix $\widehat{\mathbf{Q}}$ in equations (14) as

$$\widehat{\mathbf{Q}} = 2\ \mathrm{diag}(0, \zeta_1\omega_1, \ldots, 0, \zeta_r\omega_r)$$

matrix $\mathbf{P} > 0$ becomes

$$\mathbf{P} = \mathrm{diag}(\omega_1^2, 1, \ldots, \omega_r^2, 1)$$

The matrices $\mathbf{R}$ and $\mathbf{Q}_1 > 0$ (eq. (16)) were chosen to be diagonal and their elements were the control design variables. The dissipative LQG problem is essentially a dynamic dissipative controller as in equations (7) and (8), with the compensator matrices $\mathbf{G}_p$ and $\mathbf{G}_r = 0$ and

$$\mathbf{A}_c = \mathbf{A} - \mathbf{B}\mathbf{R}^{-1}\mathbf{B}^T\mathbf{P}_c - \mathbf{P}_f\mathbf{C}^T\mathbf{V}_m^{-1}\mathbf{C}$$

$$\mathbf{B}_c = \mathbf{P}_f\mathbf{C}^T\mathbf{V}_m^{-1}$$

$$\mathbf{G} = \mathbf{R}^{-1}\mathbf{B}^T\mathbf{P}_c$$

Thus, the closed-loop equations are the same as in equations (30). The number of modes used in the control design model for each case depended on the number of significant modes in the input-output characterization of the structure. For the phase-0 CEM, a 21-mode model was used as the plant model and the optimal control design variables, namely, 42 diagonal elements of $\mathbf{Q}_1$ followed by 6 diagonal elements of $\mathbf{R}$, are shown in table IX. For the control-optimized dissipative LQG compensator of the phase-1 CEM, an 18-mode model was used and the optimal control design variables, 36 diagonal elements of $\mathbf{Q}_1$ followed by 6 diagonal elements of $\mathbf{R}$, are shown in table X. Figure 8 shows a comparison of the maximum and minimum singular-value plots of LQG dissipative controllers for the phase-0 CEM (dashed lines) and phase-1 CEM (solid lines). As in figure 7, observation reveals that the controller gains for phase 1 are less than the controller gains for phase 0 throughout the entire frequency spectrum. However, the shapes of the controller power distributions are different for the two structures. Analytical results show that to maintain an rms LOS pointing performance of 2.0 in., the phase-0 CEM requires a control power of 5.93 lb^2, whereas the phase-1 CEM requires only 2.65 lb^2. Thus, even though dissipative LQG controllers were not used for integrated design, the overall performance improvement of the system leads to a reduction in control effort of more than 45 percent.

These results suggest that even though the integrated redesign of the phase-1 CEM involved only static and dynamic dissipative controllers, the design process made the resulting structure more amenable

for active control with alternate control design strategies as well.

Experimental Verification

Integrated Design Validation

Although numerous numerical studies in the literature have demonstrated the benefits of controls-structures integrated design, the benefits have not been experimentally demonstrated. The primary thrust of this effort was to verify by experiment the advantage of the integrated design methodology as observed in analytical studies. Of course, the paramount difficulty in experimental verification is that some assumptions made in the analytical developments are not necessarily valid in the laboratory. In the following paragraphs, some of these issues are discussed.

As mentioned earlier, dissipative system theory requires that the sensors and actuators be collocated. This collocation was not truly possible, but the sensors and actuators were located so close together (within the bays at the six control stations) that they could be considered collocated for all practical purposes. Second, the continuous time framework has been used in the dissipative theory to demonstrate guaranteed stability robustness, whereas the implementation in the laboratory was digital. The theoretical framework breaks down with discretization of the continuous time plant and controllers but because the sampling rates used were much faster than the control bandwidths, the effects of discretization become negligible.

Sensor and actuator dynamics have been ignored in the integrated design. Though no appreciable dynamics are associated with the accelerometers, the bidirectional gas thrusters experimentally exhibited first-order dynamics of the form $110/(s+273)$. However, actuator bandwidth, implied by these dynamics, was much larger than the control bandwidths (2–5 Hz) considered, so that the actuator dynamics could be ignored. Also, the velocity signals required for the controllers were obtained by integration of the accelerometer signals with the aid of washout filters, which were used to remove the constant bias in the accelerometer signal.

White-noise disturbances were assumed in the integrated design and analysis. However, for the experimental work, band-limited white noise was used because the thrusters have limited power. The bandwidth for the white noise employed was large enough to cover the controller bandwidth, so that for these control experiments the noise may be treated as white noise. Again, integrated design and analysis assumes continuous white noise, whereas in the experiments the noise was discretized at the sampling rates of the control implementation. The disturbance sequence used for the tests was made as large as possible within the maximum safety limit and the maximum power available from the disturbance actuators. At each time step the noise levels were normally distributed and were uncorrelated to all other time steps.

A computer simulation model for the laboratory structure, incorporating all the issues detailed above, was developed using MATLAB software. The mode shapes for the plant model in the simulation were obtained from a detailed NASTRAN model of the structure. System identification tests had been performed to obtain experimental modal frequency and damping values. (See ref. 11.) The system identification tests involved a significant amount of structural motion, which induced additional damping due to the motion of hoses attached to the air thrusters and other such nonlinearities. Therefore, the identified modal damping values are expected to be greater than those in the disturbance rejection experiments wherein much less motion was observed. The plant model for the simulations included modes up to 50 Hz (about 80 modes) compared with about 30 modes for control design, along with the experimentally identified damping values. The compensator system matrices for simulations were exactly those that were loaded in the real-time control software. Finally, the excitation-control scenarios and the digital implementations for the simulations were identical to those used in the experiments. The goal was to obtain a simulation of the laboratory experiment that could be used to evaluate our ability to predict actual test structure performance.

In the test sequence the controller was to turn on from the start for initialization to remove accelerometer bias and to ensure that the structure was at rest for zero initial conditions. Then the disturbance was introduced at stations 1 and 2. After 60 sec (about 4 to 5 time constants of the slowest mode) for the transients to settle, data were collected for the steady-state analysis. The applied control effort and the LOS measurements obtained from the experiments were analyzed and compared with the simulations for each test case. Exactly the same experiments were conducted on the nominal phase-0 CEM and the redesigned phase-1 CEM. Figures 9–18 show the results of control experiments with the static dissipative controller, figures 19–28 represent the dynamic dissipative results, and figures 29–38 summarize the results for dissipative LQG control experiments.

The control inputs at station 3 with the static dissipative controllers for the phase-0 CEM and the phase-1 CEM are shown for comparison in figures 9(a) and 9(b), respectively. The time axis of these figures starts at 60 sec because the earlier data are ignored for steady-state analysis. The digital implementation of the static dissipative controllers is at 200 Hz, so 60 sec of data yields 12 000 time steps. When the control input sequence for an experimental run is denoted $\mathbf{u}_i(k)$ ($i = 1, \ldots, 6$ and $k = 1, \ldots, 12\,000$), a running average for the control power is computed as

$$\mathrm{pow}(k) = \frac{1}{(k-1)} \sum_{j=1}^{k} \left[\sum_{i=1}^{6} \mathbf{u}_i^2(j) \right] \tag{31}$$

This running average is plotted for static dissipative controllers in figure 18, in figure 28 for dynamic dissipative controllers, and in figure 38 for dissipative LQG controllers.

The deviations of the laser point on the detector system from its nominal position in the local X and Y Cartesian coordinates are shown in figures 15 and 16 for the static dissipative controller. Figures 15(a) and 16(a) are for phase-0 CEM; figures 15(b) and 16(b) are for the phase-1 CEM. Denoting these observations as $X(k)$ and $Y(k)$ for $k = 1, \ldots, 12\,000$, a running rms LOS error was computed as follows:

$$\mathrm{rms}(k) = \left\{ \frac{1}{(k-1)} \sum_{j=1}^{k} \left[X^2(j) + Y^2(j) \right] \right\}^{\frac{1}{2}} \tag{32}$$

The rms LOS pointing error is plotted for the static dissipative controllers in figure 17. Figures 27 and 37 show similar plots for dynamic dissipative and dissipative LQG controllers, respectively. Due to the relatively higher order of the dissipative LQG controllers, the sampling rate for experiments with these controllers had to be reduced to 125 Hz.

The results for static dissipative controllers are shown in figures 9–18. A comparison of the control inputs at stations 3–8 is shown in figures 9–14, with the phase-0 control input in figures 9(a)–14(a) and the phase-1 CEM control input in figures 9(b)–14(b). The output LOS pointing errors in the X and Y directions for the phase-0 CEM and the phase-1 CEM are shown in figures 15 and 16, respectively. Figure 17 shows that the rms LOS pointing error for both structures is approximately equal to 0.6 in. Note that the experimentally observed value of rms pointing error is 0.6 in. rather than the analytically computed value of 2.4 in. because discrete time, band-limited noise was used for the disturbance input at actuators 1 and 2 in the experiments, whereas the analytical work assumed continuous white noise. The difference in rms pointing error values for the phase-0 CEM and the phase-1 CEM can be attributed to the resolution of the laser detector system in the laboratory, which is 0.2 in. Figure 18 illustrates the average control power needed to maintain this LOS pointing error. The control power in the experiment for the phase-0 CEM was nearly 2 V^2, whereas that for the phase-1 CEM is 0.66 V^2, a reduction of about 77 percent. The simulations for these experimental runs show a decrease in control effort from 1.56 V^2 for the phase-0 CEM to 0.73 V^2 for the phase-1 CEM (reduction of about 53 percent), which is closer to that predicted by the analysis. However, the decrease in control power observed experimentally was more than that predicted by analysis. Figure 18 shows that the control power level predicted by simulation for the phase-1 CEM matches the experimental level quite well. However, this match is not the case for the phase-0 CEM. In fact, the control power level computed by simulations is about 28 percent off from the experimental counterpart. This disparity may be attributed to the spillover excitation of the modes outside the 5-Hz control bandwidth, to the modes not having been parameterized accurately, and to other modeling errors.

Figures 19–28 display the results for experiments with dynamic dissipative controllers. Figures 19–24 compare the control input at stations 3–8 for the two structures, whereas figures 25 and 26 compare the deviations of the laser from its nominal position in the X and Y directions. The experimental verification of the advantages of integrated design for dynamic dissipative controllers is observed in figures 27 and 28. As seen in figure 27, the rms LOS pointing performance is maintained near 0.6 in. for both structures and the simulation results are consistent. The average control power of 1.65 V^2 for the phase-0 CEM was reduced to 0.64 V^2 for the phase-1 CEM, a reduction of 75 percent. (See fig. 28.) The simulations show the reduction of control power from 1.35 V^2 for the phase-0 CEM to 0.7 V^2 for the phase-1 CEM (reduction of about 49 percent), which is closer to the analytical predictions. Again, the difference between the experimental and simulation predictions may be attributed to the spillover effects from the unmodeled dynamics of the flexible structure. A comparison of figures 18 and 28 also reveals that dynamic dissipative controllers needed less control power than the static dissipative controller to maintain the same

LOS pointing performance for both structures, as predicted by the analysis. (See table II.)

Therefore, the experimental results show that the benefits of integrated design predicted analytically are achieved experimentally. Also, the experiment showed that the integrated controls-structures design can provide an overall design that requires much less control power to achieve the same pointing performance to that obtained through the conventional design approach. This power savings makes the integrated controls-structures design superior to the conventional design.

Experimental Results for Alternate Controller

The results of the disturbance rejection experiments with control-optimized dissipative LQG controllers are given in figures 29–38. The control effort input at stations 3–8 are shown for the phase-0 CEM and the phase-1 CEM in figures 29–34; the LOS pointing errors are shown in figures 35 and 36. Similar to the static and dynamic dissipative results, a comparison of the levels of control power for the phase-0 CEM and the phase-1 CEM in figures 29–34 shows that the phase-1 CEM requires less control power to maintain the allowable rms pointing performance. Further, this savings is confirmed in figure 38, which is a plot of the average control power for these experiments. To maintain the rms LOS at 0.5 in., the control power needed for the phase-0 CEM was 1.16 V^2, which is reduced to 0.44 V^2 for the phase-1 CEM. The reduction in control power is about 62 percent. In simulations, the control power was reduced from 0.94 V^2 for the phase-0 CEM to 0.36 V^2 for the phase-1 CEM, a reduction of about 62 percent.

These experiments confirm the analytical observation that the integrated design structure, the phase-1 CEM, requires considerably less control power with dissipative LQG controllers than the phase-0 CEM, even though the integrated design process employed static and dynamic dissipative control strategies. Thus, along with optimization of control power with the selected control design strategy, the integrated design process makes the resulting structure more amenable to control with alternate control strategies.

Concluding Remarks

Experimental validation of an optimization-based integrated controls-structures design approach has been presented for two types of dissipative controllers. The nominal phase-0 Controls-Structures-Interaction (CSI) Evolutionary Model (CEM) structure was redesigned to minimize the average control power required to maintain a specified root-mean-square line-of-sight pointing performance under persistent disturbances. The redesigned structure, the phase-1 CEM, was assembled in the laboratory and tested in comparison with the phase-0 CEM. Two different dissipative controllers were used—the static dissipative controller and the dynamic dissipative controller—to obtain a reduction in control power of more than 60 percent while the same line-of-sight pointing performance was maintained. This increase in performance has been observed both analytically and experimentally. Therefore, analytical and experimental tests have demonstrated that the integrated controls-structures design can yield designs that are substantially superior to those obtained through the traditional sequential approach. Although numerous analytical/numerical studies in the literature suggest benefits derived from the controls-structures integrated design, this is the first experimental verification of such performance enhancements. Moreover, experiments with dissipative linear-quadratic Gaussian controllers indicate that the integrated design process made the structure more amenable to active control, such that superior overall designs may be achieved with alternate control design strategies as well. Finally, this work demonstrates the capability of the software design tool CSI-DESIGN to implement the automated design procedure in a unified environment for structural and control designs.

NASA Langley Research Center
Hampton, VA 23681-0001
September 8, 1994

References

1. Ketner, G. L.: *Survey of Historical Incidences With Controls-Structures Interaction and Recommended Technology Improvements Needed to Put Hardware in Space.* PNL-6846 (Contract DE-AC06-76RLO 1830), Battelle Memorial Inst., Mar. 1989.

2. Joshi, S. M.: *Control of Large Flexible Space Structures—Lecture Notes in Control and Information Sciences.* M. Thoma and A. Wyner, eds., Volume 131, Springer-Verlag, 1989.

3. Newsom, Jerry R.; Layman, W. E.; Waites, H. B.; and Hayduk, R. J.: *The NASA Controls-Structures Interaction Technology Program.* IAF-90-290, Oct. 1990.

4. Rao, S. S.; and Pan, T. S.: *Robustness Improvement of Actively Controlled Structures Through Integrated Structural/Control Design.* WL-TR-91-3058, U.S. Air Force, May 21, 1991.

5. Maghami, P. G.; Joshi, S. M.; Armstrong, E. S.; and Walz, J. E.: Integrated Controls—Structures Design Methodology Development for a Class of Flexible Spacecraft. *Third Air Force/NASA Symposium on Recent Advances in Multidisciplinary Analysis and Optimization—A Collection of Technical Papers*, Sept. 1990, pp. 1–6.

6. Maghami, Peiman G.; Joshi, Suresh M.; and Armstrong, Ernest S.: *An Optimization-Based Integrated Controls-Structures Design Methodology for Flexible Space Structures.* NASA TP-3283, 1993.

7. Woodard, Stanley E.; Padula, Sharon L.; Graves, Philip C.; and James, Benjamin B.: An Optimization Method for Controlled Space Structures With Variable Actuator Mass. *Proceedings of the Fourth NASA/DOD Control/Structures Interaction Technology Conference*, Andrew D. Swanson, compiler, WL-TR-91-3013, U.S. Air Force, Jan. 1991, pp. 411–428. (Available from DTIC as AD A235 843.)

8. Joshi, S. M.; and Maghami, P. G.: Dissipative Compensators for Flexible Spacecraft Control. *IEEE Trans. Aerosp. & Elect. Sys.*, vol. 28, no. 3, July 1992, pp. 768–774.

9. Lefschetz, Solomon: *Stability of Nonlinear Control Systems.* Academic Press Inc., 1965.

10. Lozano-Leal, R.; and Joshi, S. M.: On the Design of Dissipative LQG-Type Controllers. *Recent Advances in Robust Control*, Peter Dorato and Rama K. Yedavalli, eds., IEEE, 1990, pp. 251–252.

11. Belvin, W. Keith; Elliott, Kenny B.; Horta, Lucas G.; Bailey, Jim P.; Bruner, Anne M.; Sulla, Jeffrey L.; Won, John; and Ugoletti, Roberto M.: *Langley's CSI Evolutionary Model: Phase 0.* NASA TM-104165, 1991.

12. Stengel, Robert F.: *Stochastic Optimal Control—Theory and Application.* John Wiley & Sons, Inc., 1986.

13. Vanderplaats, G. N.: *ADS—A FORTRAN Program for Automated Design Synthesis—Version 1.10.* NASA CR-177985, 1985.

14. Armstrong, Ernest S.: *ORACLS—A System for Linear-Quadratic-Gaussian Control Law Design.* NASA TP-1106, 1978.

15. Dongarra, J. J.; Bunch, J. R.; Moler, C. B.; and Stewart, G. W.: *LINPACK Users' Guide.* SIAM, 1979.

16. Belvin, W. Keith; and Park, K. C.: Computer Implementation of Analysis and Optimization Procedures for Control-Structure Interaction Problems. *A Collection of Technical Papers—AIAA Dynamics Specialist Conference*, Apr. 1990, pp. 32–41. (Available as AIAA-90-1194.)

17. Vanderplaats, Garret N.: *Numerical Optimization Techniques for Engineering Design—With Applications.* McGraw-Hill, Inc., 1984.

18. George, Alan; and Liu, Joseph W.-H.: *Computer Solution of Large Sparse Positive Definite Systems.* Prentice-Hall, Inc., 1981.

19. Kenny, Sean P.; Hou, Gene J.; and Belvin, W. Keith: Eigensensitivity in Integrated Design. *Proceedings of the Fourth NASA/DOD Control/Structures Interaction Technology Conference*, Andrew D. Swanson, compiler, WL-TR-91-3013, U.S. Air Force, Jan. 1991, pp. 31–40. (Available from DTIC as AD A235 843.)

Table I. Modal Frequencies of Phase-0 CEM

Mode	Frequency, Hz
1	0.1471
2	.1491
3	.1552
4	.7300
5	.7478
6	.8739
7	1.4730
8	1.7379
9	1.8821
10	2.2938

Table II. Results of Design Study With Static and Dynamic Dissipative Controllers

[rms LOS = 2.4 in.]

Design	Control power, lb^2
Control optimized with static dissipative controller	7.11
Integrated with static dissipative controller	4.21
Control optimized with dynamic dissipative controller	6.41
Integrated with dynamic dissipative controller	3.64

Table III. Structural Design Variables for Integrated Design With Static Dissipative Controllers

Variable	Area, in^2	Description	Section
Longerons			
1	0.330	Main truss	1
4	.085	Horizontal boom	2
7	.173	Laser tower	3
10	.260	Main truss	4
13	.257	Main truss	5
16	.095	Horizontal boom	6
19	.096	Reflector tower	7
Battens			
2	0.082	Main truss	1
5	.083	Horizontal boom	2
8	.082	Laser tower	3
11	.082	Main truss	4
14	.081	Main truss	5
17	.081	Horizontal boom	6
20	.081	Reflector tower	7
Diagonals			
3	0.082	Main truss	1
6	.085	Horizontal boom	2
9	.082	Laser tower	3
12	.081	Main truss	4
15	.079	Main truss	5
18	.079	Horizontal boom	6
21	.082	Reflector tower	7

Table IV. Control Design Variables for Integrated Design With Static Dissipative Controllers

Variable	Control-optimized design	Integrated design	Actuator
1	1.2110	0.5586	3
2	2.0634	.6837	4
3	1.2985	.7899	5
4	.5352	1.1117	6
5	1.5050	1.0201	7
6	.4593	.5982	8

Table V. Structural Design Variables for Integrated Design
With Dynamic Dissipative Controllers

Variable	Area, in^2	Description	Section
Longerons			
1	0.330	Main truss	1
4	.080	Horizontal boom	2
7	.142	Laser tower	3
10	.295	Main truss	4
13	.258	Main truss	5
16	.100	Horizontal boom	6
19	.117	Reflector tower	7
Battens			
2	0.077	Main truss	1
5	.087	Horizontal boom	2
8	.086	Laser tower	3
11	.080	Main truss	4
14	.078	Main truss	5
17	.077	Horizontal boom	6
20	.083	Reflector tower	7
Diagonals			
3	0.098	Main truss	1
6	.087	Horizontal boom	2
9	.082	Laser tower	3
12	.066	Main truss	4
15	.066	Main truss	5
18	.066	Horizontal boom	6
21	.083	Reflector tower	7

Table VI. Control Design Variables for Integrated Design
With Dynamic Dissipative Controllers

Variable	Control-optimized design	Integrated design
$\mathbf{A}_c[2,1]$	136.57	135.39
$\mathbf{A}_c[2,2]$	105.25	114.73
$\mathbf{A}_c[4,3]$	136.60	301.81
$\mathbf{A}_c[4,4]$	104.33	102.17
$\mathbf{A}_c[6,5]$	103.80	80.42
$\mathbf{A}_c[6,6]$	107.72	125.07
$\mathbf{A}_c[8,7]$	94.56	58.21
$\mathbf{A}_c[8,8]$	121.26	103.52
$\mathbf{A}_c[10,9]$	136.92	95.28
$\mathbf{A}_c[10,10]$	103.87	107.26
$\mathbf{A}_c[12,11]$	100.11	136.11
$\mathbf{A}_c[12,12]$	126.11	133.30
$\mathbf{Q}[1,1]$	15 287.63	18 122.76
$\mathbf{Q}[2,2]$	30 050.42	12 173.74
$\mathbf{Q}[3,3]$	15 125.39	10 430.10
$\mathbf{Q}[4,4]$	29 103.43	13 600.71
$\mathbf{Q}[5,5]$	19 640.50	24 674.52
$\mathbf{Q}[6,6]$	24 331.62	19 487.68
$\mathbf{Q}[7,7]$	20 582.68	22 964.97
$\mathbf{Q}[8,8]$	22 159.79	21 224.58
$\mathbf{Q}[9,9]$	15 148.89	22 693.96
$\mathbf{Q}[10,10]$	29 362.52	20 381.06
$\mathbf{Q}[11,11]$	20 009.49	17 783.45
$\mathbf{Q}[12,12]$	21 511.89	15 376.09

Table VII. Effective Areas of Struts for Fabricated Phase-1 CEM

Variable	Area, in^2	Description	Section
Longerons			
1	0.333	Main truss	1
4	.099	Horizontal boom	2
7	.175	Laser tower	3
10	.264	Main truss	4
13	.264	Main truss	5
16	.099	Horizontal boom	6
19	.099	Reflector tower	7
Battens			
2	0.097	Main truss	1
5	.097	Horizontal boom	2
8	.097	Laser tower	3
11	.097	Main truss	4
14	.097	Main truss	5
17	.097	Horizontal boom	6
20	.097	Reflector tower	7
Diagonals			
3	0.083	Main truss	1
6	.083	Horizontal boom	2
9	.083	Laser tower	3
12	.083	Main truss	4
15	.083	Main truss	5
18	.083	Horizontal boom	6
21	.083	Reflector tower	7

Table VIII. Modal Frequencies for Fabricated Phase-1 CEM

Mode	Frequency, Hz
1	0.1475
2	.1495
3	.1553
4	.7320
5	.7517
6	.8890
7	1.4817
8	2.2449
9	2.4042
10	2.5298

Table IX. Design Variables for Control-Optimized Dissipative LQG Controller; Phase-0 CEM

Variable	Control-optimized design
$\mathbf{Q}_1[1,1]$	14 508.45
$\mathbf{Q}_1[2,2]$	357 188.60
$\mathbf{Q}_1[3,3]$	5 139.08
$\mathbf{Q}_1[4,4]$	53 364.76
$\mathbf{Q}_1[5,5]$	0
$\mathbf{Q}_1[6,6]$	377 416.22
$\mathbf{Q}_1[7,7]$	40 424.27
$\mathbf{Q}_1[8,8]$	3 046 328.32
$\mathbf{Q}_1[9,9]$	105 444.24
$\mathbf{Q}_1[10,10]$	0
$\mathbf{Q}_1[11,11]$	4 573.37
$\mathbf{Q}_1[12,12]$	177.63
$\mathbf{Q}_1[13,13]$	0
$\mathbf{Q}_1[14,14]$	3.67
$\mathbf{Q}_1[15,15]$	0
$\mathbf{Q}_1[16,16]$	0
$\mathbf{Q}_1[17,17]$	0
$\mathbf{Q}_1[18,18]$	5 700.42
$\mathbf{Q}_1[19,19]$	2 919.63
$\mathbf{Q}_1[20,20]$	58.74
$\mathbf{Q}_1[21,21]$	1 035.00
$\mathbf{Q}_1[22,22]$	3.10
$\mathbf{Q}_1[23,23]$	.98
$\mathbf{Q}_1[24,24]$	1.27
$\mathbf{Q}_1[25,25]$	0
$\mathbf{Q}_1[26,26]$	1.08
$\mathbf{Q}_1[27,27]$	1.21
$\mathbf{Q}_1[28,28]$	8.58
$\mathbf{Q}_1[29,29]$	1.21
$\mathbf{Q}_1[30,30]$	1.43
$\mathbf{Q}_1[31,31]$	6.58
$\mathbf{Q}_1[32,32]$	5.14
$\mathbf{Q}_1[33,33]$	0
$\mathbf{Q}_1[34,34]$	9.33
$\mathbf{Q}_1[35,35]$	7.77
$\mathbf{Q}_1[36,36]$	0
$\mathbf{Q}_1[37,37]$	0
$\mathbf{Q}_1[38,38]$	0
$\mathbf{Q}_1[39,39]$	16.23
$\mathbf{Q}_1[40,40]$	11.40
$\mathbf{Q}_1[41,41]$	0
$\mathbf{Q}_1[42,42]$	0
$\mathbf{R}[1,1]$	.81
$\mathbf{R}[2,2]$	.95
$\mathbf{R}[3,3]$	.49
$\mathbf{R}[4,4]$	.79
$\mathbf{R}[5,5]$	.53
$\mathbf{R}[6,6]$	1.56

Table X. Design Variables for Control-Optimized Dissipative LQG Controller; Phase-1 CEM

Variable	Control-optimized design
$\mathbf{Q}_1[1,1]$	19 171.70
$\mathbf{Q}_1[2,2]$	219 407.96
$\mathbf{Q}_1[3,3]$	660.41
$\mathbf{Q}_1[4,4]$	0
$\mathbf{Q}_1[5,5]$	136 116.82
$\mathbf{Q}_1[6,6]$	37 841.48
$\mathbf{Q}_1[7,7]$	134 339.60
$\mathbf{Q}_1[8,8]$	72 793.13
$\mathbf{Q}_1[9,9]$	71 028.80
$\mathbf{Q}_1[10,10]$	1 899.28
$\mathbf{Q}_1[11,11]$	1 062.82
$\mathbf{Q}_1[12,12]$	1 194.98
$\mathbf{Q}_1[13,13]$	0
$\mathbf{Q}_1[14,14]$	0
$\mathbf{Q}_1[15,15]$	795.54
$\mathbf{Q}_1[16,16]$	1 021.76
$\mathbf{Q}_1[17,17]$	1 008.20
$\mathbf{Q}_1[18,18]$	989.86
$\mathbf{Q}_1[19,19]$	1.04
$\mathbf{Q}_1[20,20]$	1.00
$\mathbf{Q}_1[21,21]$	.99
$\mathbf{Q}_1[22,22]$	0
$\mathbf{Q}_1[23,23]$	1.00
$\mathbf{Q}_1[24,24]$	.98
$\mathbf{Q}_1[25,25]$	.97
$\mathbf{Q}_1[26,26]$	.95
$\mathbf{Q}_1[27,27]$	1.00
$\mathbf{Q}_1[28,28]$	2.27
$\mathbf{Q}_1[29,29]$	1.14
$\mathbf{Q}_1[30,30]$	1.42
$\mathbf{Q}_1[31,31]$	0
$\mathbf{Q}_1[32,32]$	0
$\mathbf{Q}_1[33,33]$	0
$\mathbf{Q}_1[34,34]$	1.13
$\mathbf{Q}_1[35,35]$	.96
$\mathbf{Q}_1[36,36]$	.90
$\mathbf{R}[1,1]$	1.57
$\mathbf{R}[2,2]$	1.19
$\mathbf{R}[3,3]$	1.02
$\mathbf{R}[4,4]$	.87
$\mathbf{R}[5,5]$	1.26
$\mathbf{R}[6,6]$	1.98

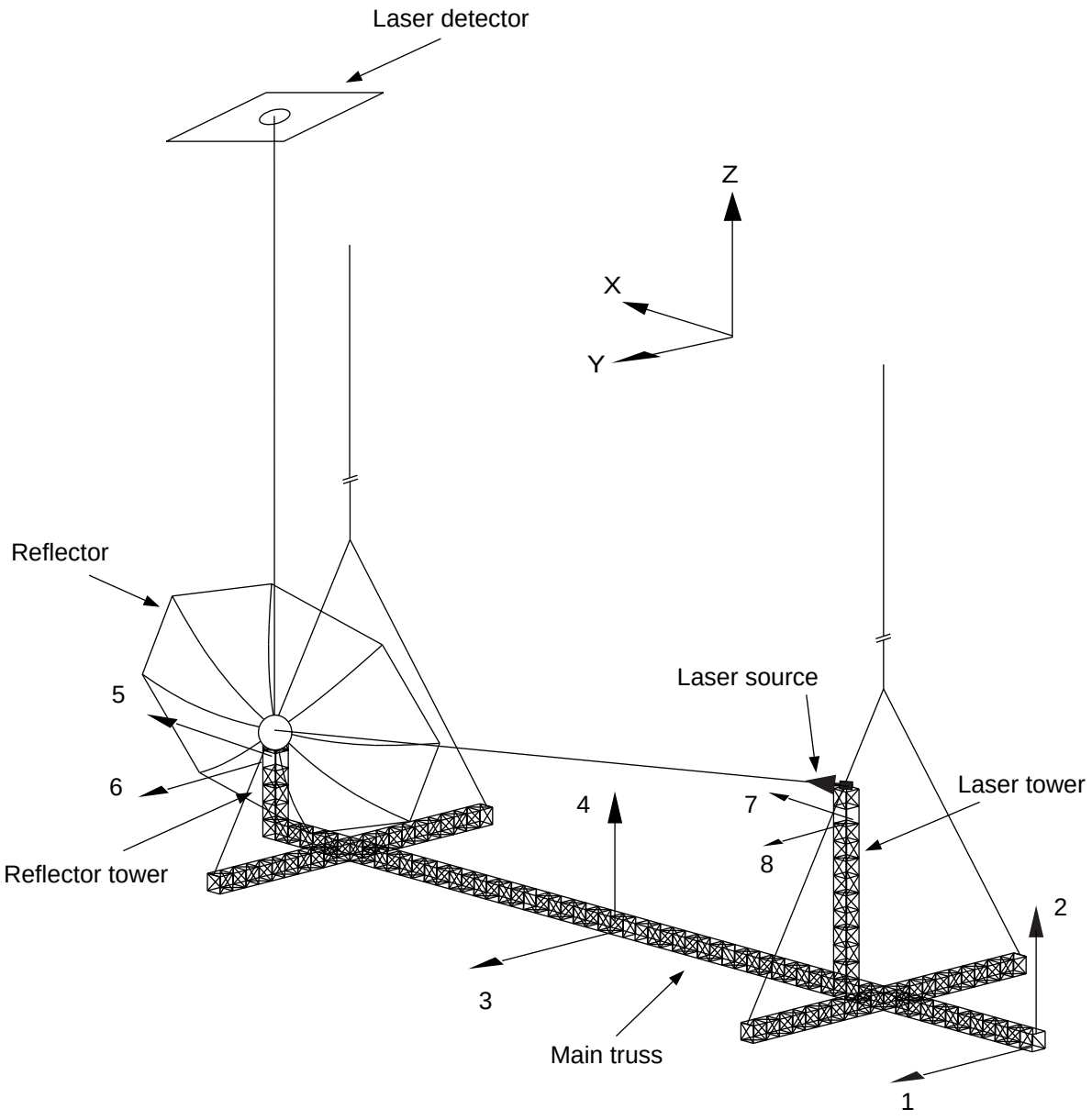

Figure 1. CEM testbed with stations 1–8 shown.

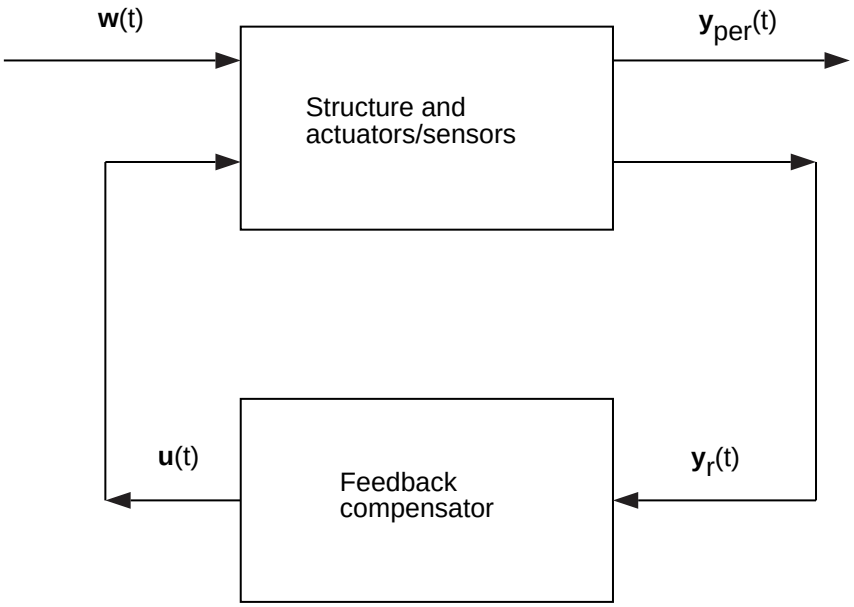

Figure 2. Feedback control configuration for integrated design.

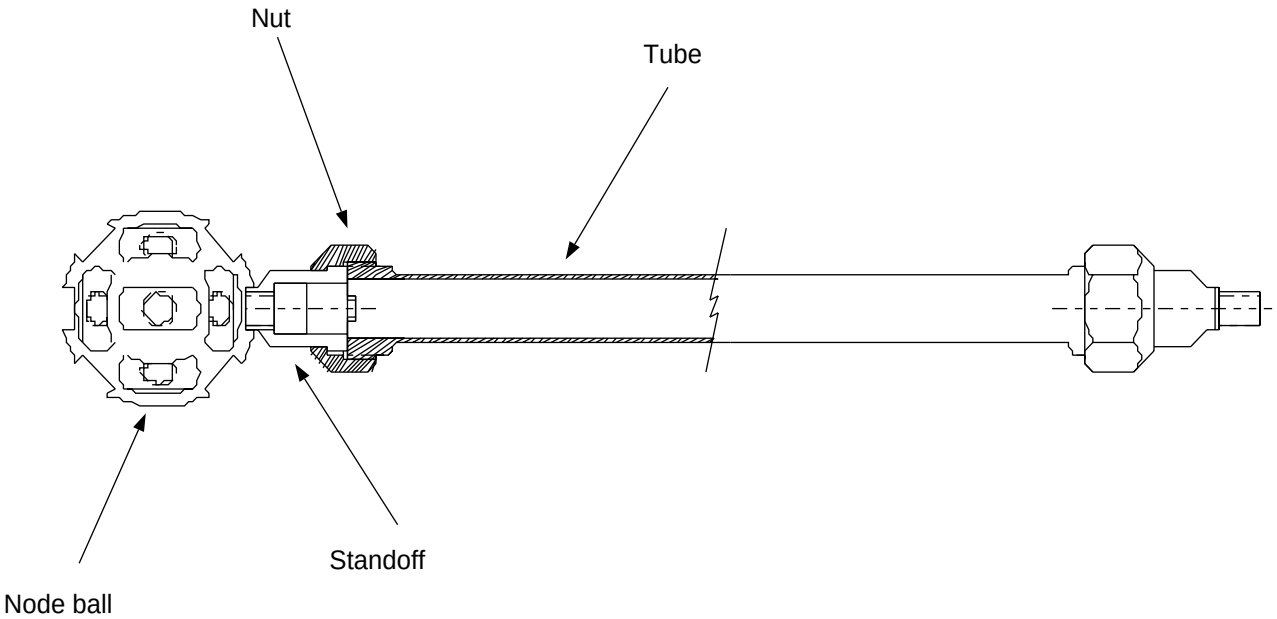

Figure 3. Strut design for phase-1 CEM.

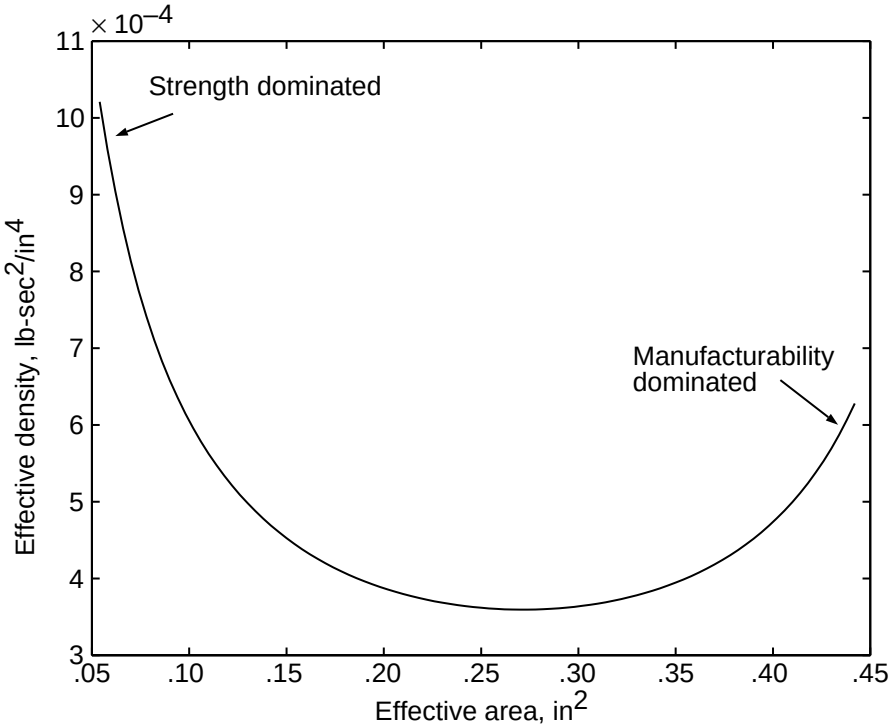

Figure 4. Strut design guide for longerons and battens.

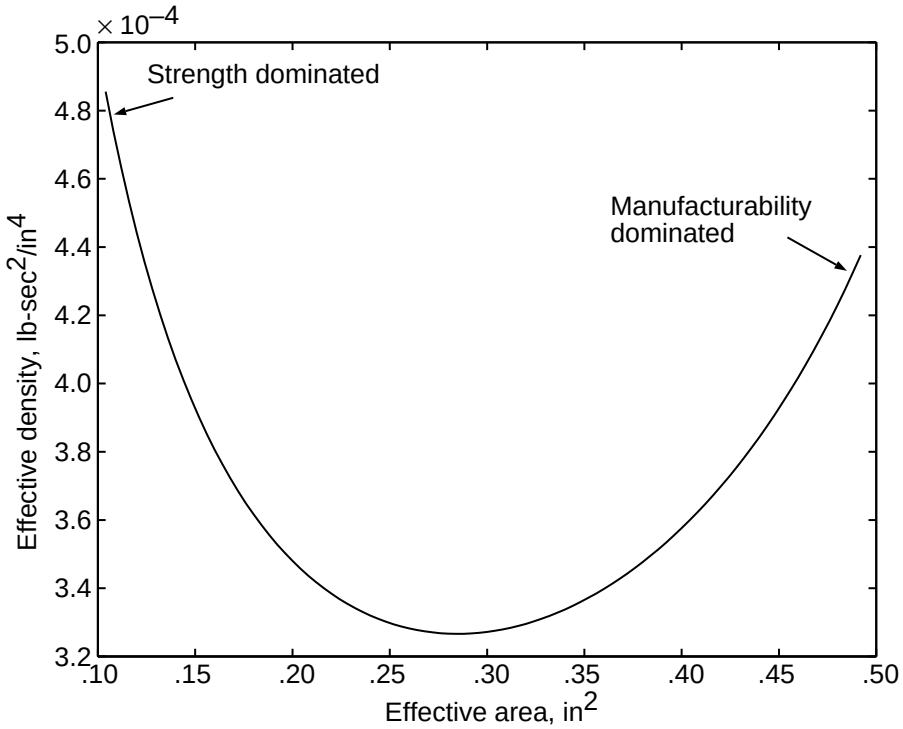

Figure 5. Strut design guide for diagonals.

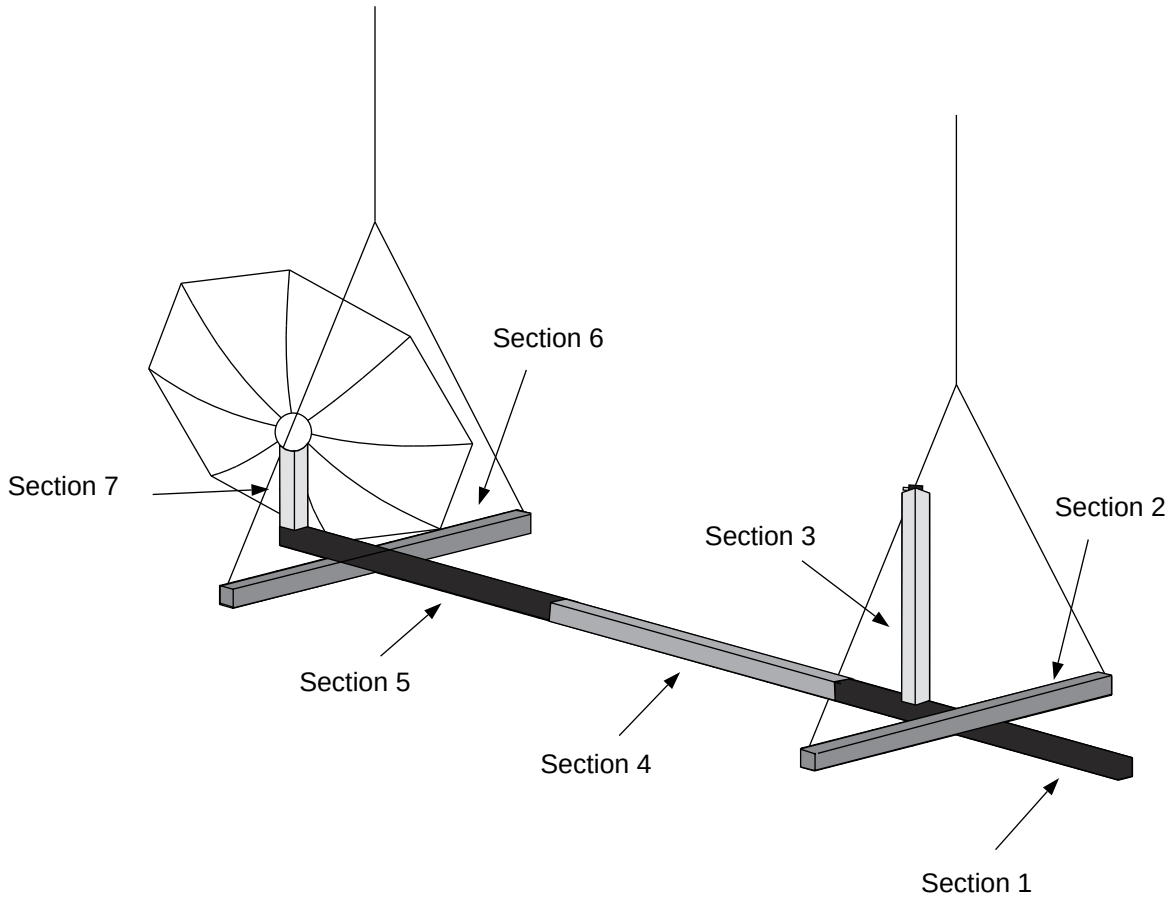

Figure 6. Seven sections of CEM model for integrated redesign.

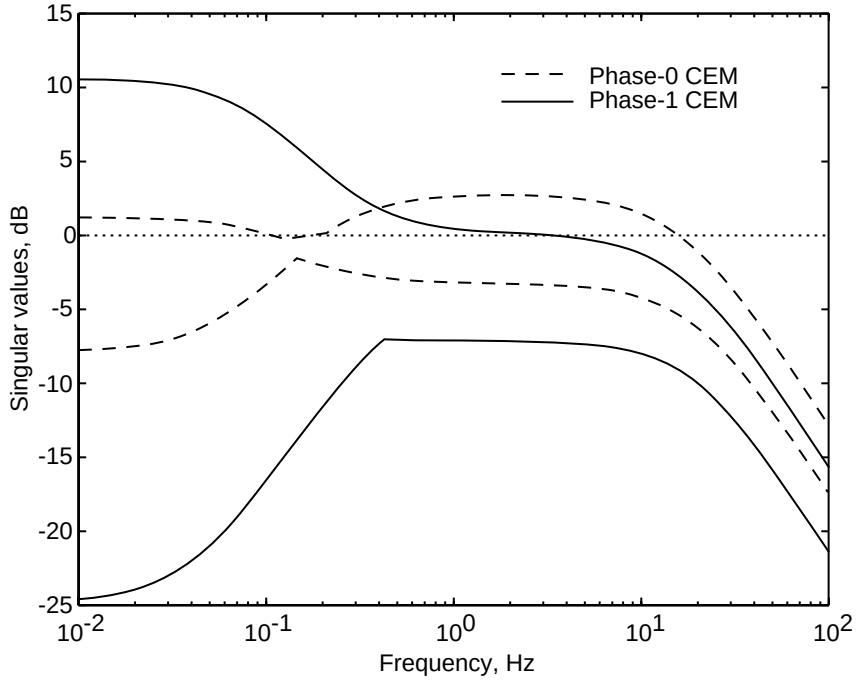

Figure 7. Maximum and minimum singular values of dynamic dissipative controllers.

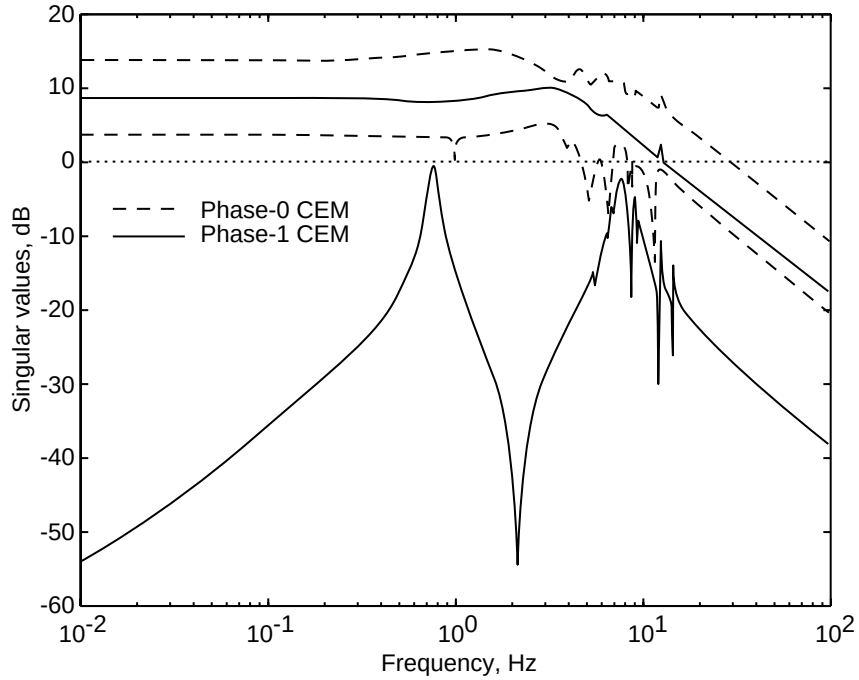

Figure 8. Maximum and minimum singular values for LQG dissipative controller.

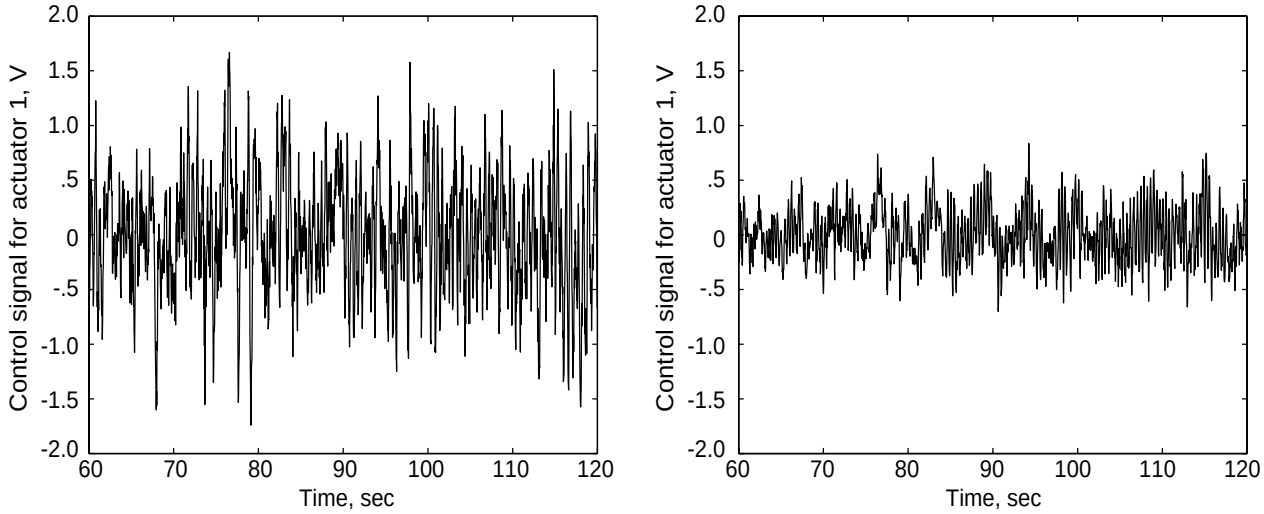

(a) Phase-0 CEM. (b) Phase-1 CEM.

Figure 9. Control signal at station 3 with static dissipative controller.

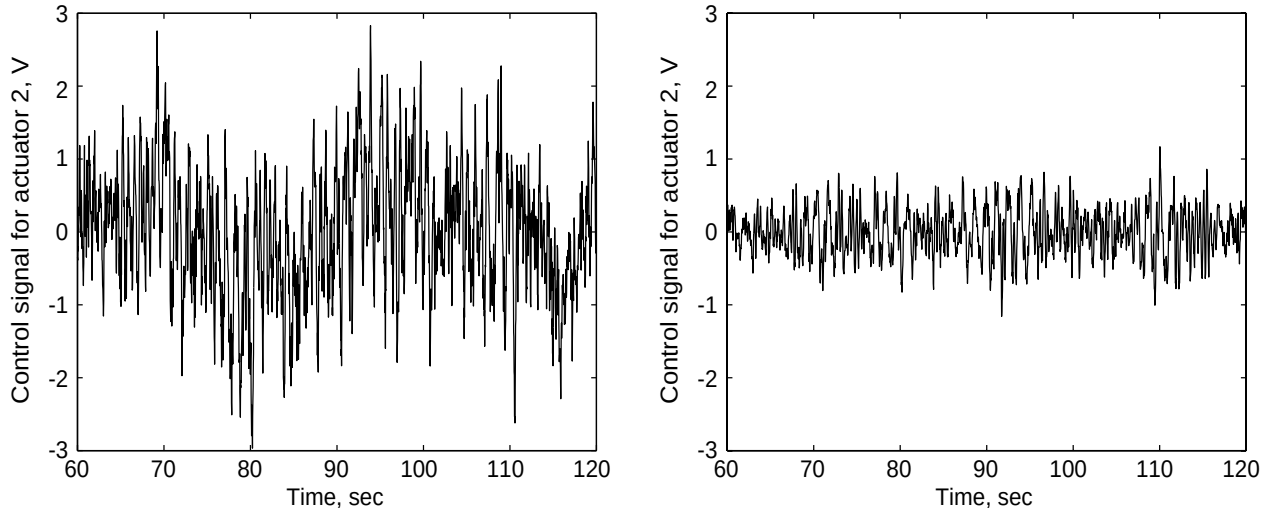

(a) Phase-0 CEM. (b) Phase-1 CEM.

Figure 10. Control signal at station 4 with static dissipative controller.

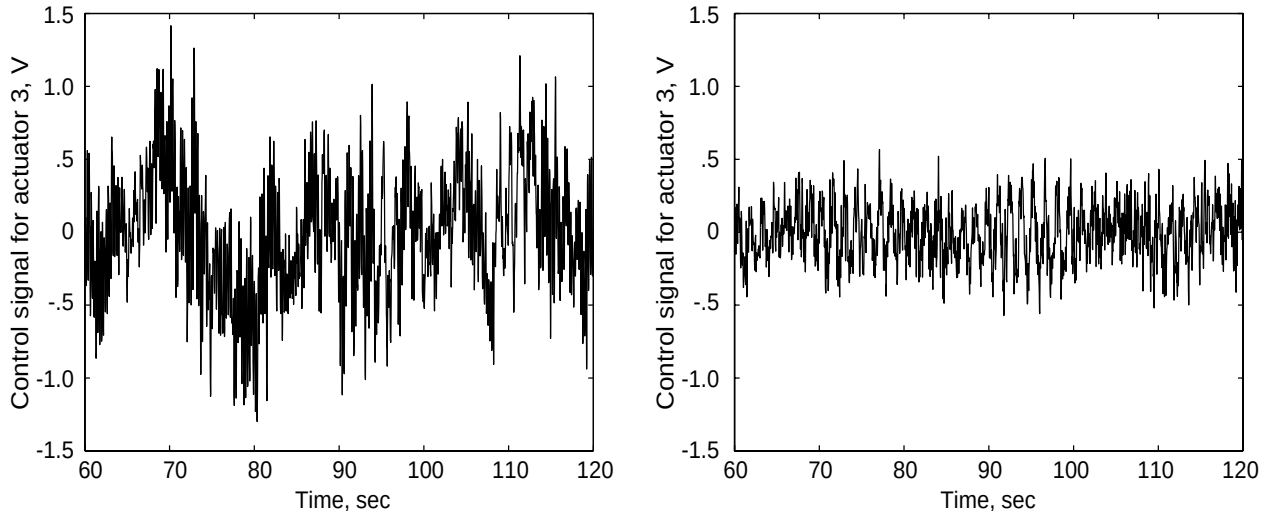

(a) Phase-0 CEM. (b) Phase-1 CEM.

Figure 11. Control signal at station 5 with static dissipative controller.

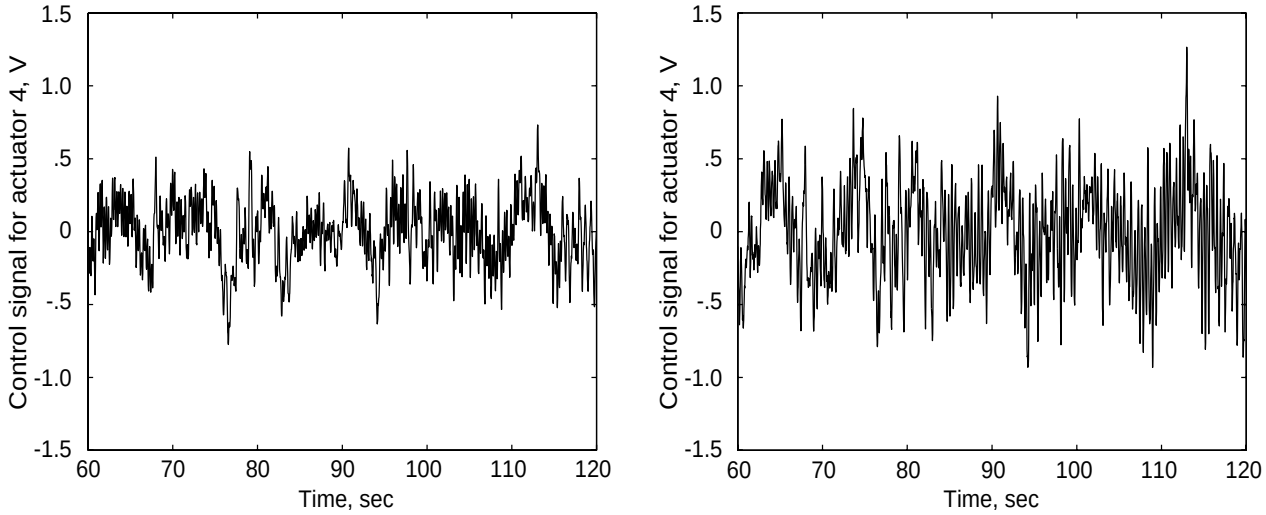

(a) Phase-0 CEM. (b) Phase-1 CEM.

Figure 12. Control signal at station 6 with static dissipative controller.

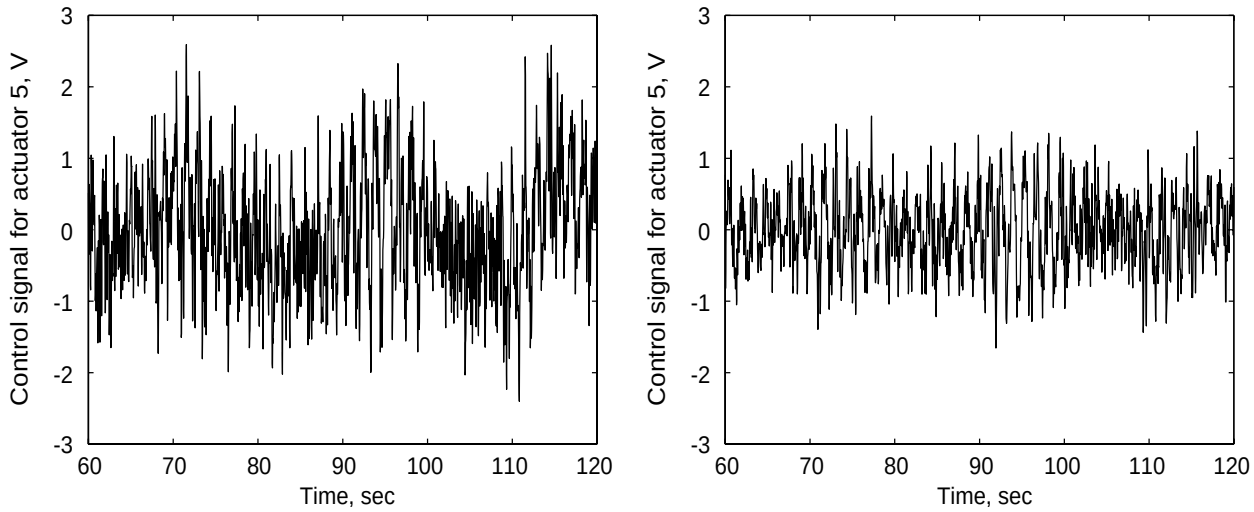

(a) Phase-0 CEM. (b) Phase-1 CEM.

Figure 13. Control signal at station 7 with static dissipative controller.

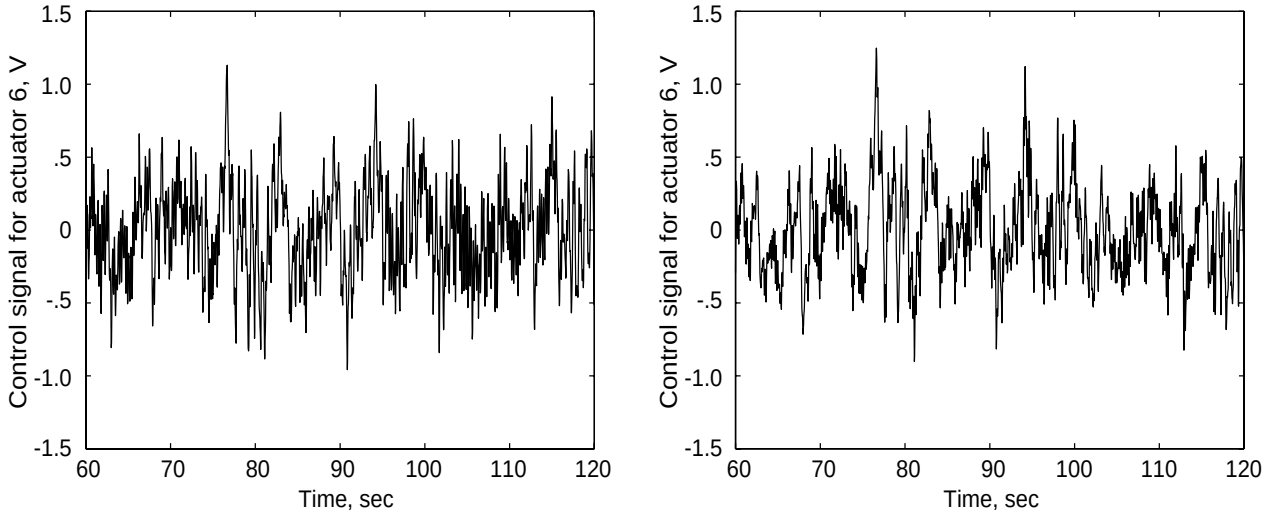

(a) Phase-0 CEM. (b) Phase-1 CEM.

Figure 14. Control signal at station 8 with static dissipative controller.

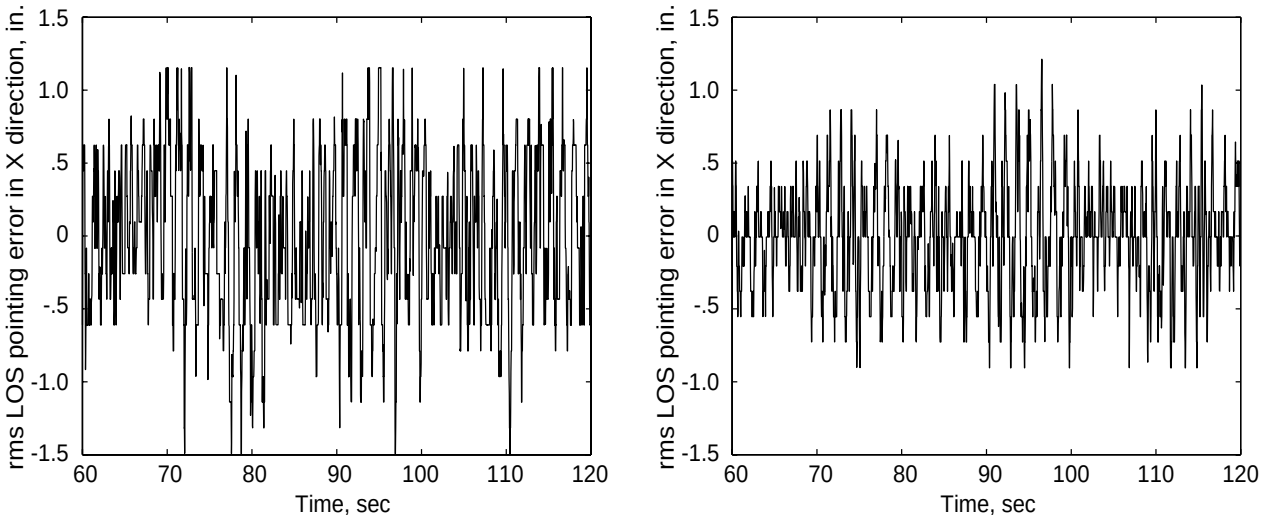

(a) Phase-0 CEM. (b) Phase-1 CEM.

Figure 15. LOS pointing error in X direction with static dissipative controller.

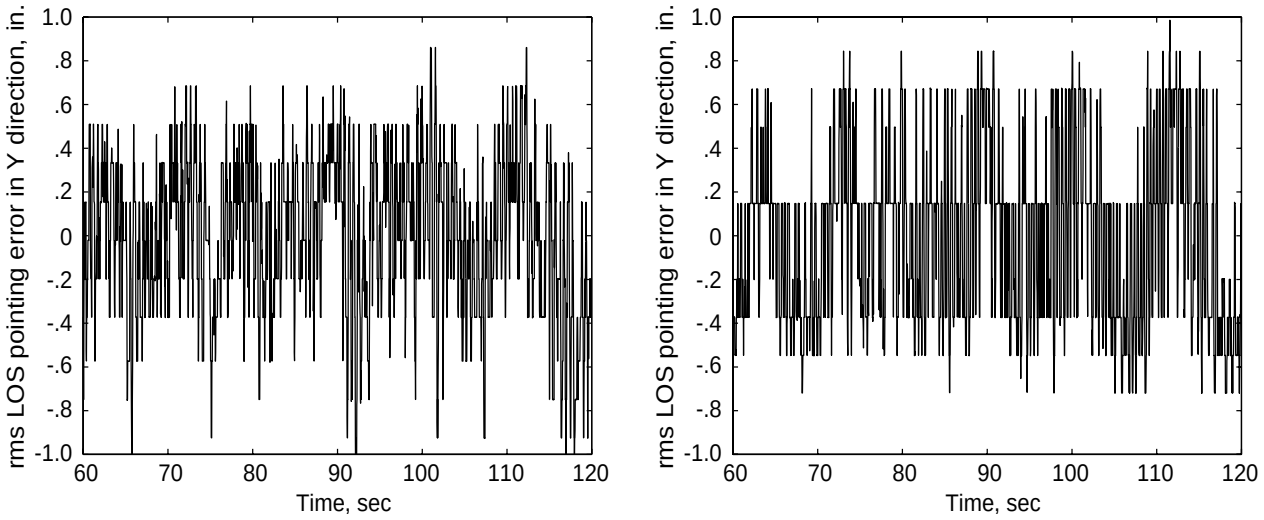

(a) Phase-0 CEM. (b) Phase-1 CEM.

Figure 16. LOS pointing error in Y direction with static dissipative controller.

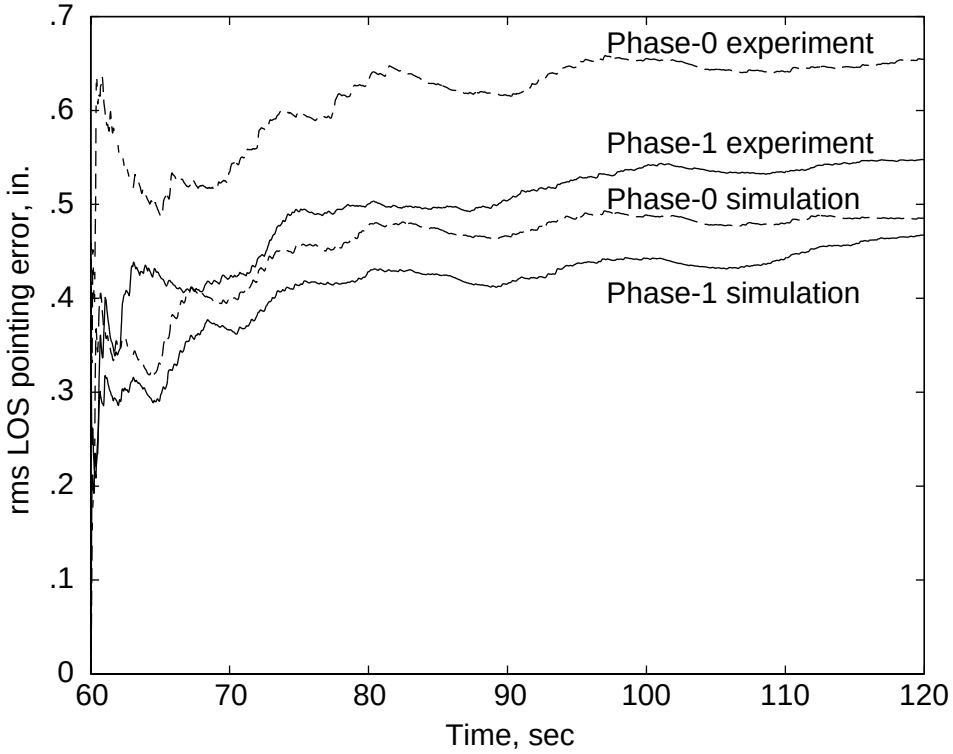

Figure 17. Comparison of rms LOS pointing error with static dissipative controllers.

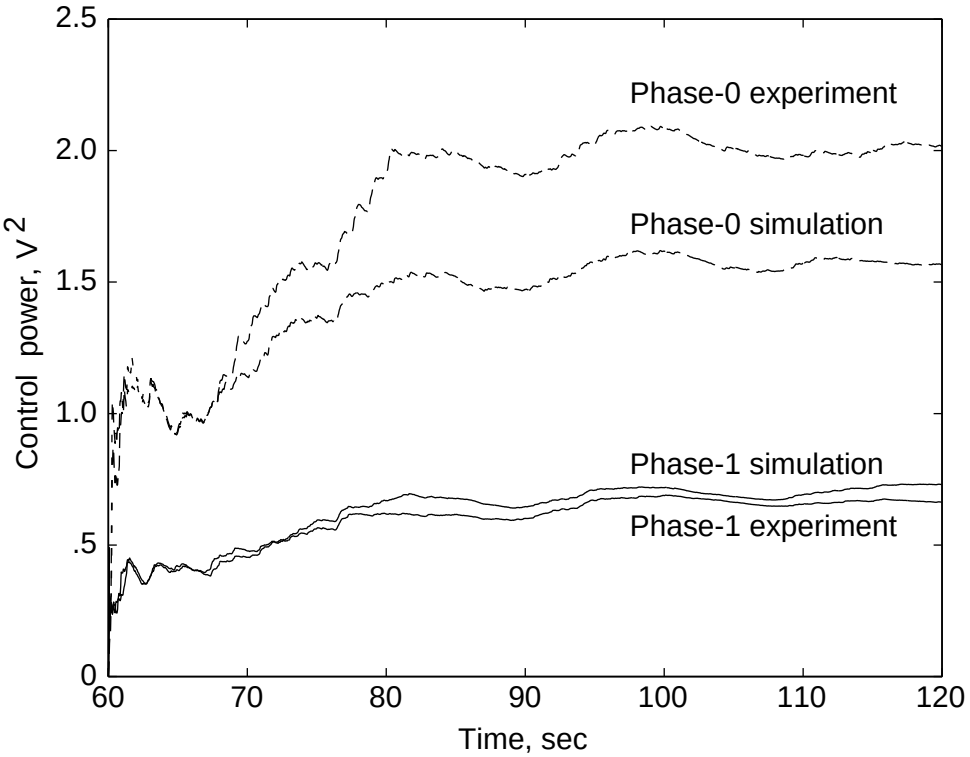

Figure 18. Comparison of average control power with static dissipative controllers.

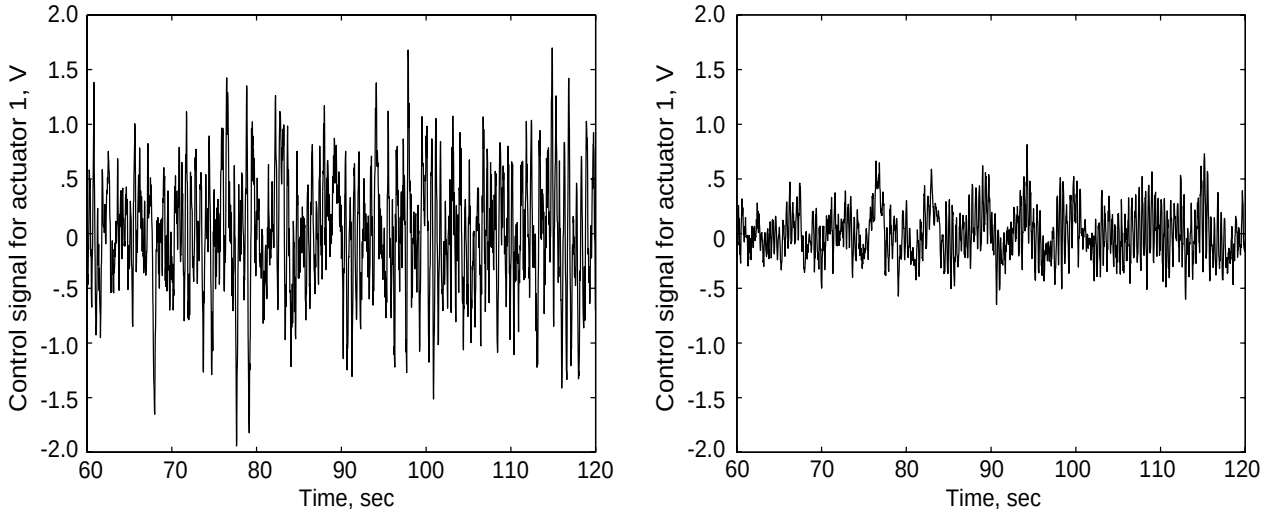

(a) Phase-0 CEM. (b) Phase-1 CEM.

Figure 19. Control signal at station 3 with dynamic dissipative controller.

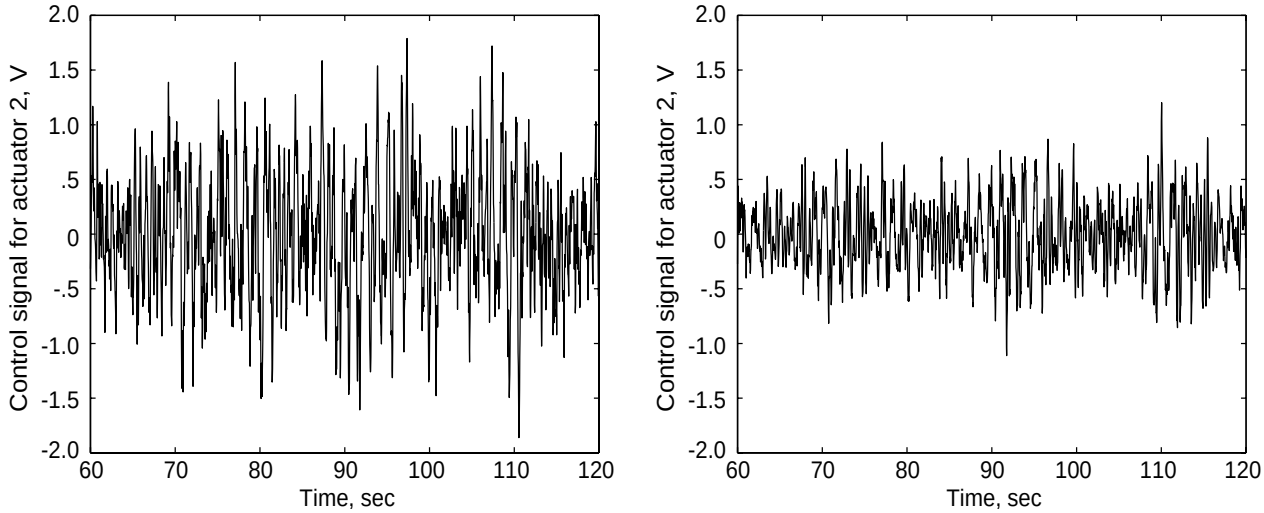

(a) Phase-0 CEM. (b) Phase-1 CEM.

Figure 20. Control signal at station 4 with dynamic dissipative controller.

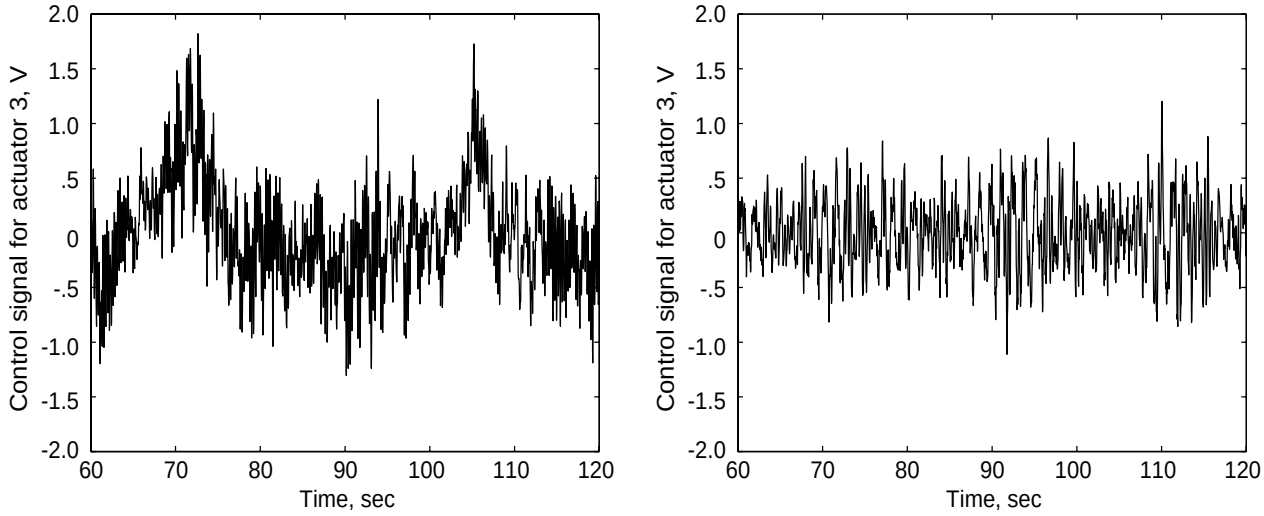

(a) Phase-0 CEM. (b) Phase-1 CEM.

Figure 21. Control signal at station 5 with dynamic dissipative controller.

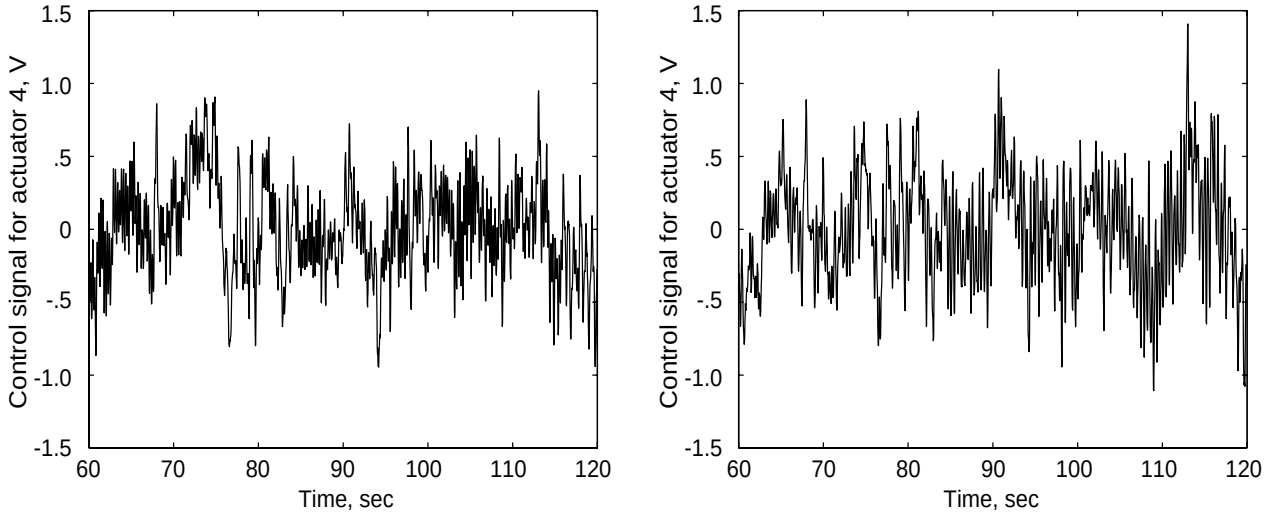

(a) Phase-0 CEM. (b) Phase-1 CEM.

Figure 22. Control signal at station 6 with dynamic dissipative controller.

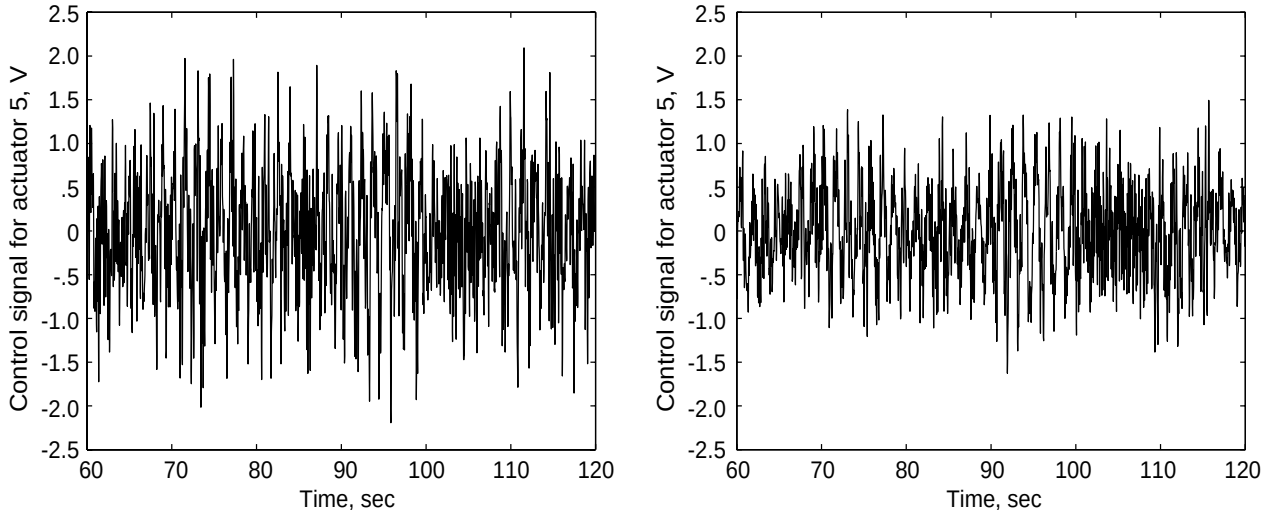

(a) Phase-0 CEM. (b) Phase-1 CEM.

Figure 23. Control signal at station 7 with dynamic dissipative controller.

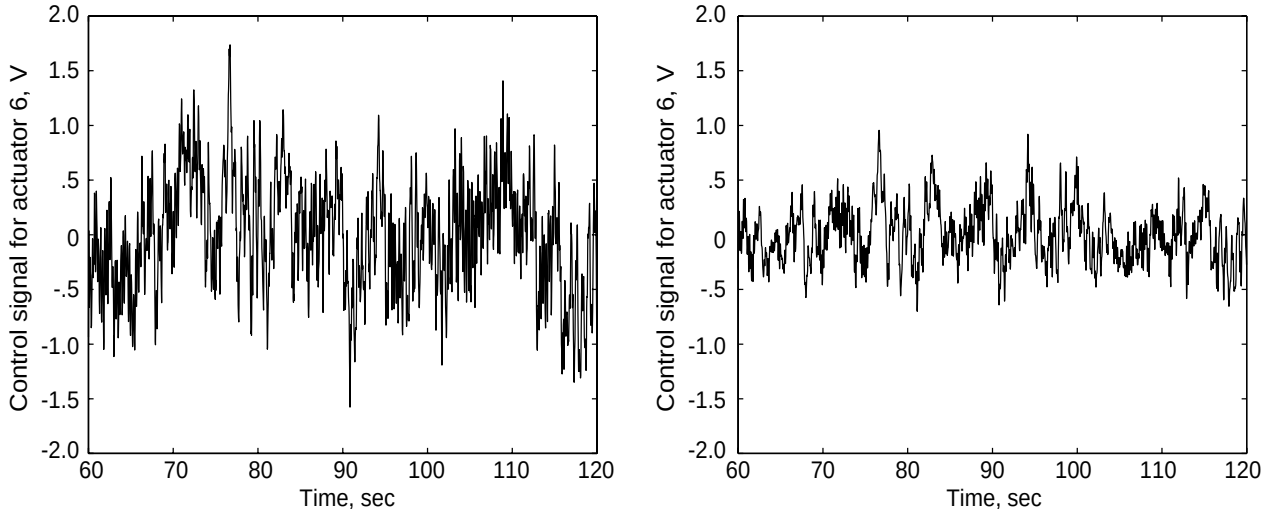

(a) Phase-0 CEM. (b) Phase-1 CEM.

Figure 24. Control signal at station 8 with dynamic dissipative controller.

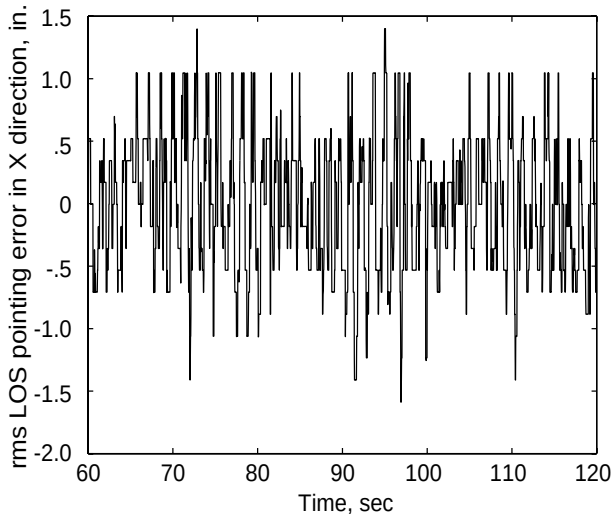

(a) Phase-0 CEM.

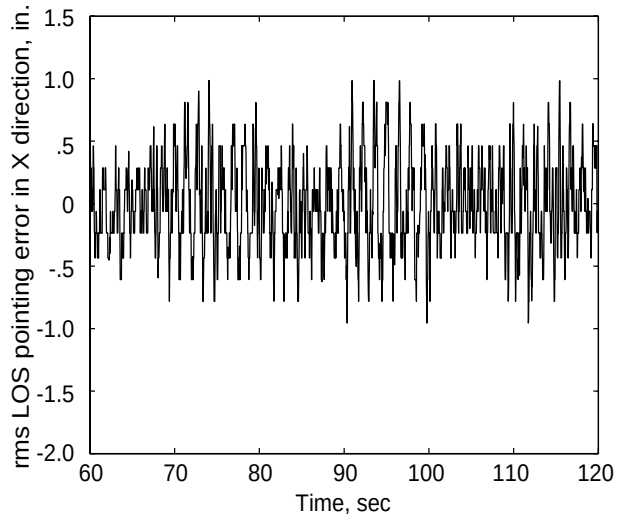

(b) Phase-1 CEM.

Figure 25. LOS pointing error in X direction with dynamic dissipative controller.

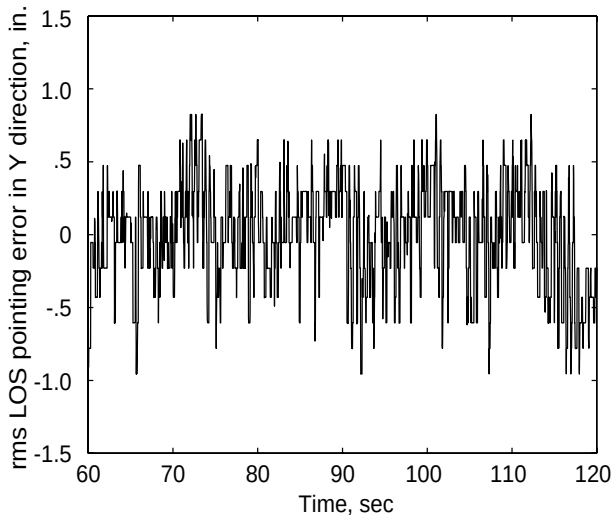

(a) Phase-0 CEM.

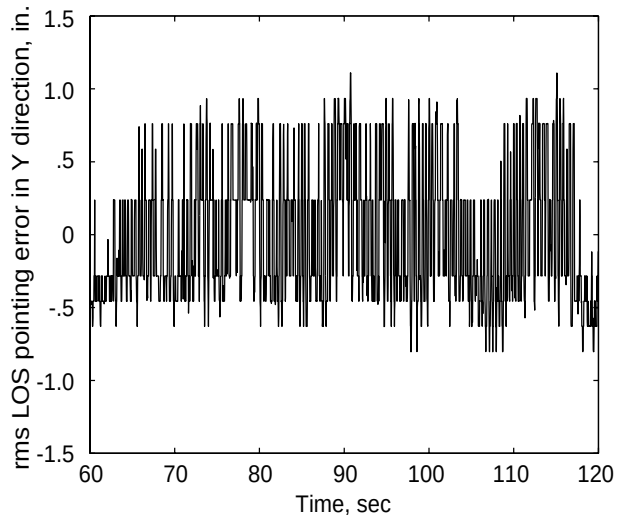

(b) Phase-1 CEM.

Figure 26. LOS pointing error in Y direction with dynamic dissipative controller.

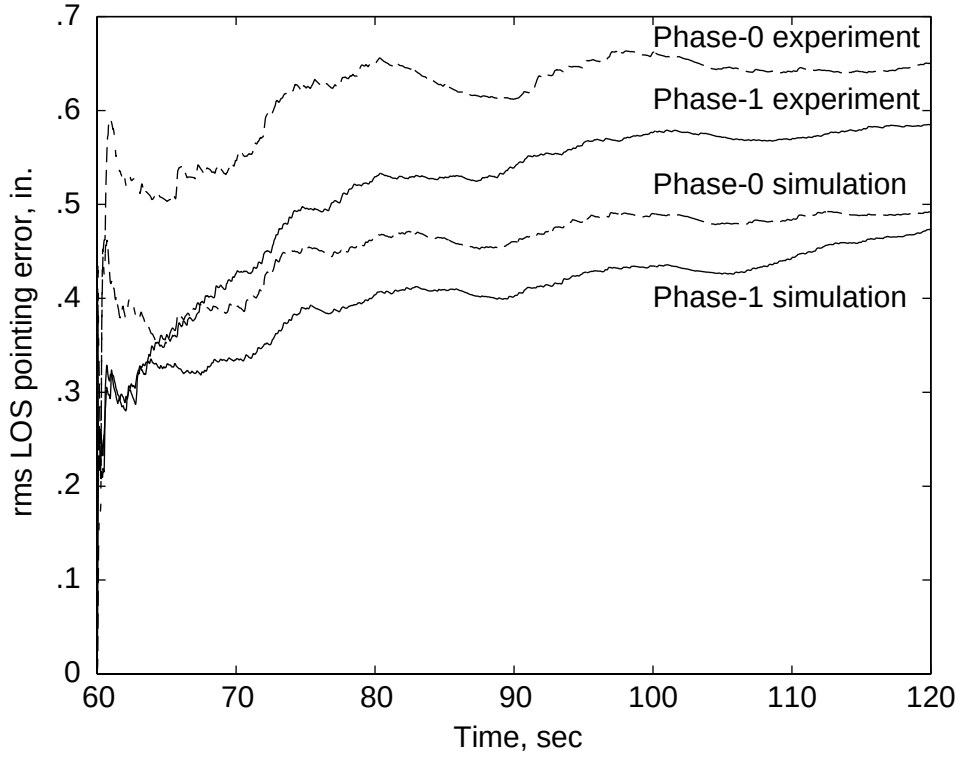

Figure 27. Comparison of rms LOS pointing error with dynamic dissipative controllers.

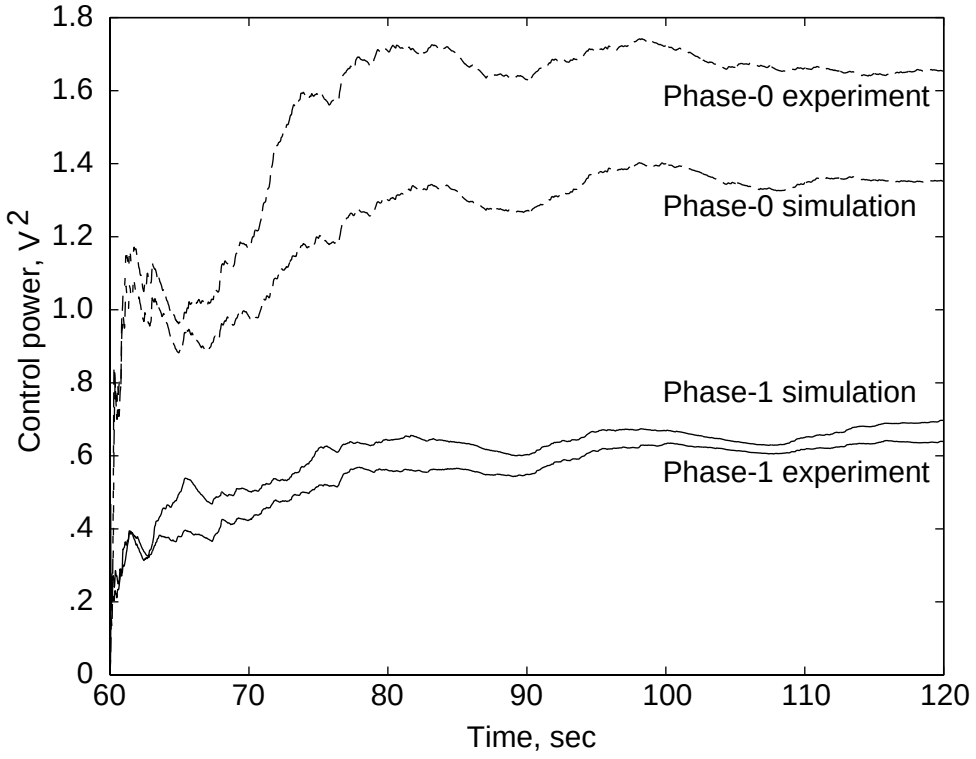

Figure 28. Comparison of average control power with dynamic dissipative controllers.

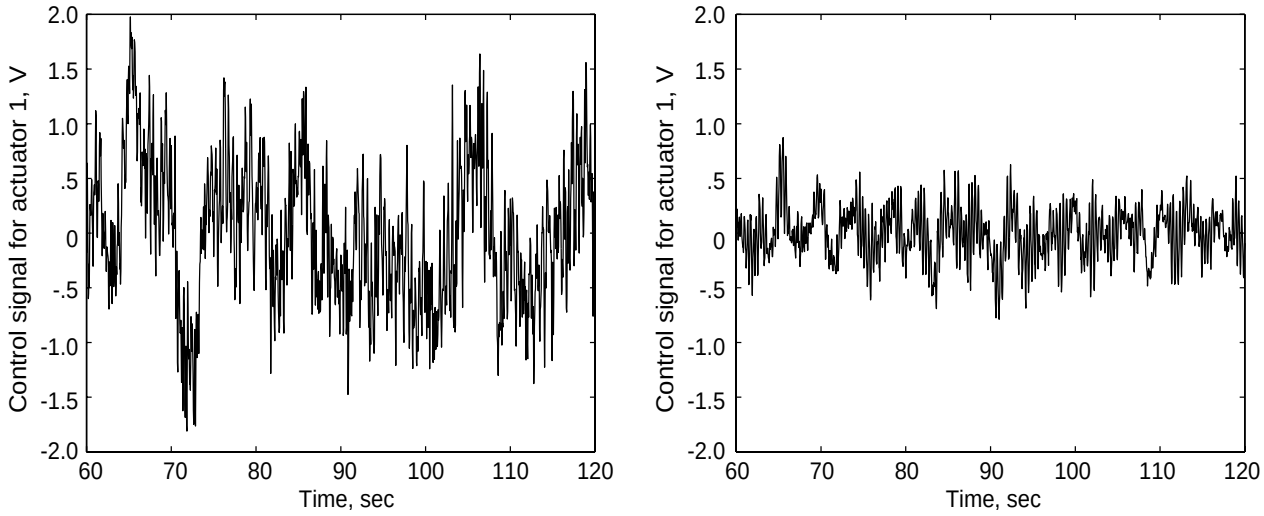

(a) Phase-0 CEM. (b) Phase-1 CEM.

Figure 29. Control signal at station 3 with dissipative LQG controller.

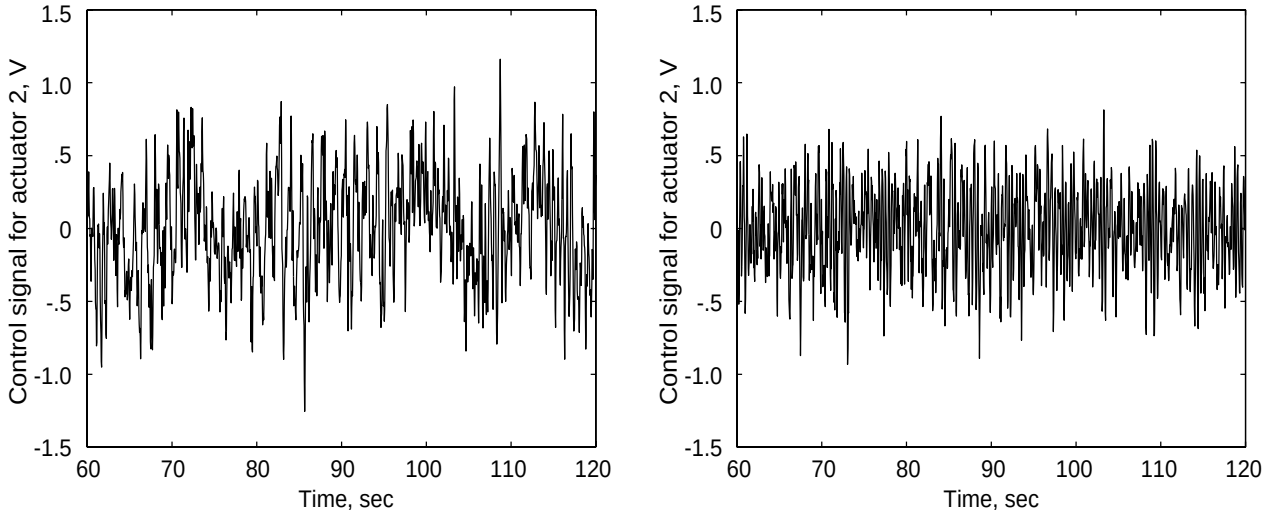

(a) Phase-0 CEM. (b) Phase-1 CEM.

Figure 30. Control signal at station 4 with dissipative LQG controller.

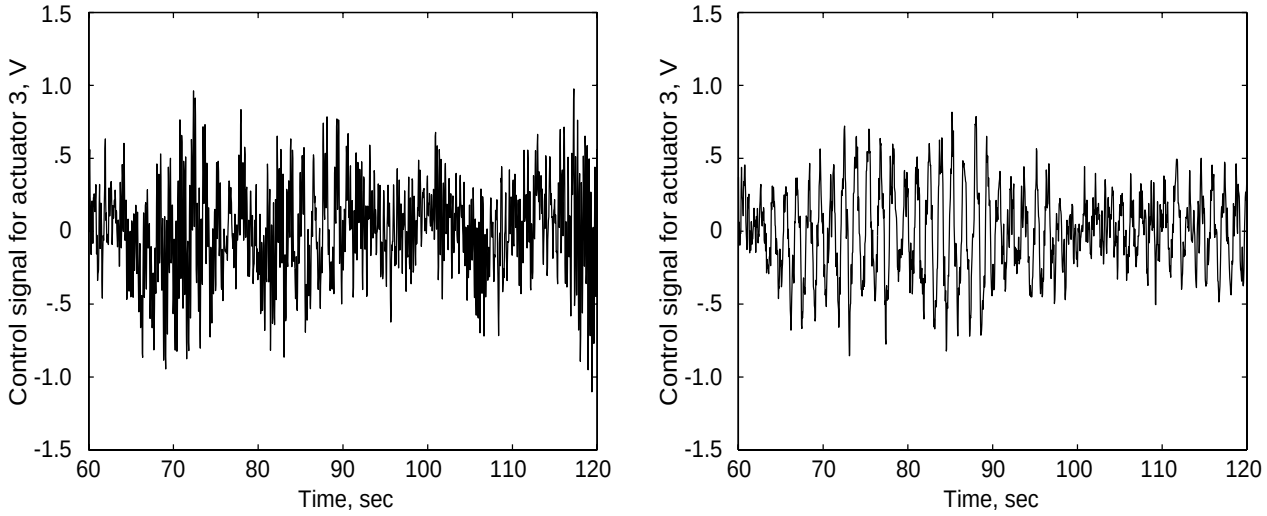

(a) Phase-0 CEM. (b) Phase-1 CEM.

Figure 31. Control signal at station 5 with dissipative LQG controller.

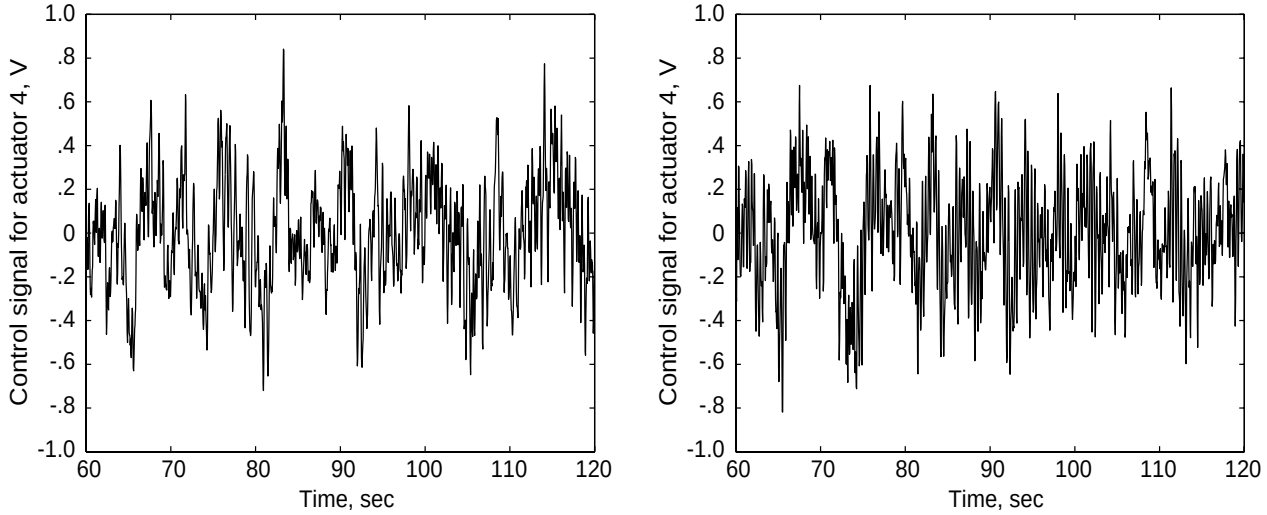

(a) Phase-0 CEM. (b) Phase-1 CEM.

Figure 32. Control signal at station 6 with dissipative LQG controller.

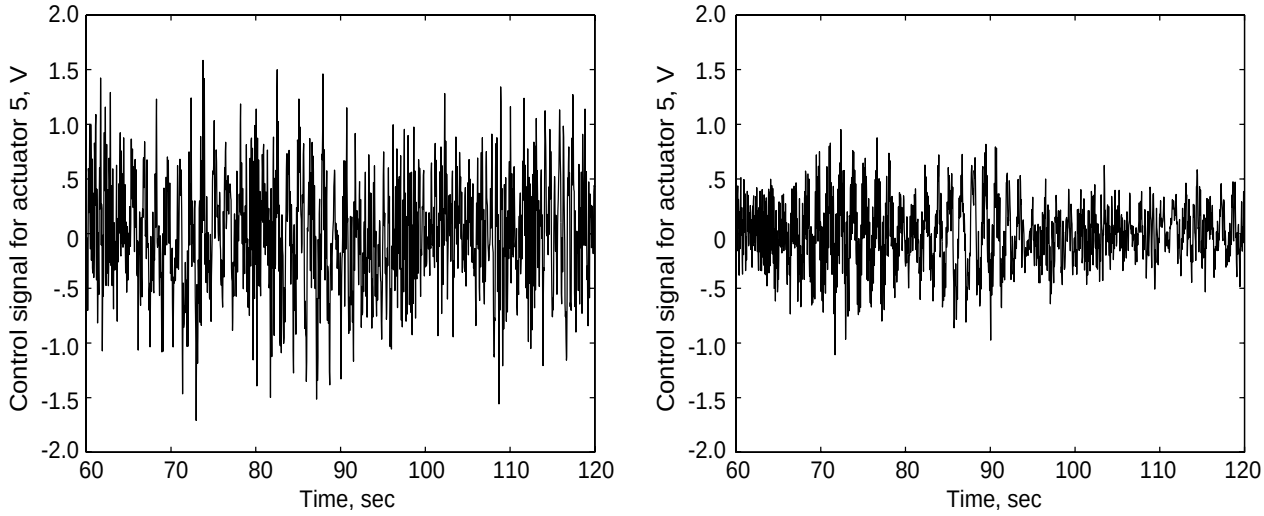

(a) Phase-0 CEM. (b) Phase-1 CEM.

Figure 33. Control signal at station 7 with dissipative LQG controller.

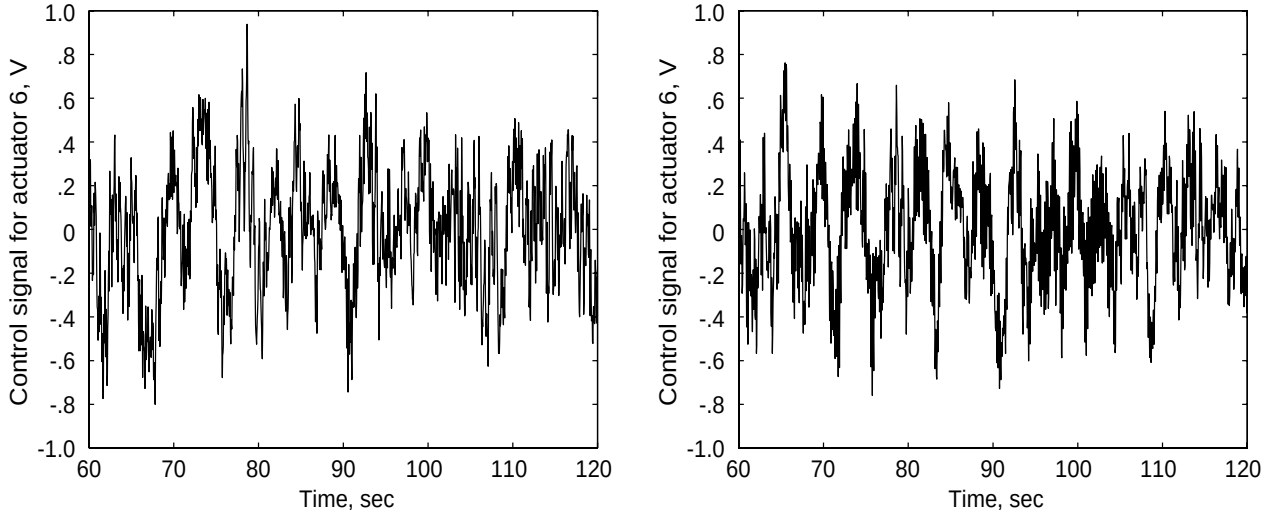

(a) Phase-0 CEM. (b) Phase-1 CEM.

Figure 34. Control signal at station 8 with dissipative LQG controller.

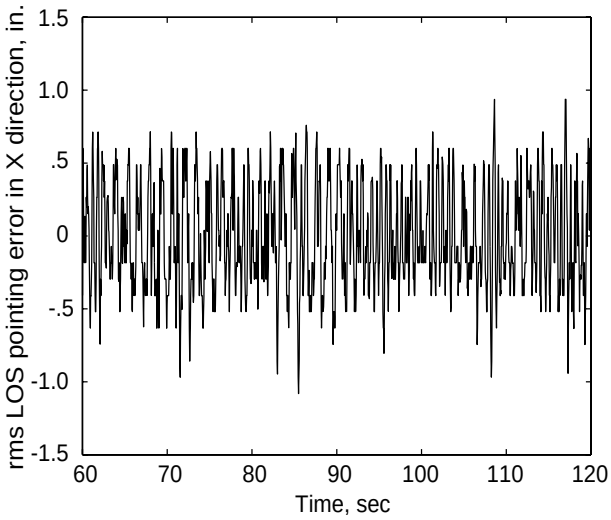

(a) Phase-0 CEM.

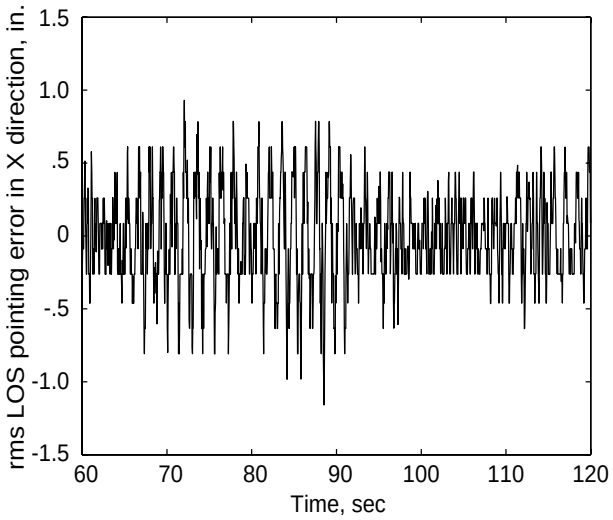

(b) Phase-1 CEM.

Figure 35. LOS pointing error in X direction with dissipative LQG controller.

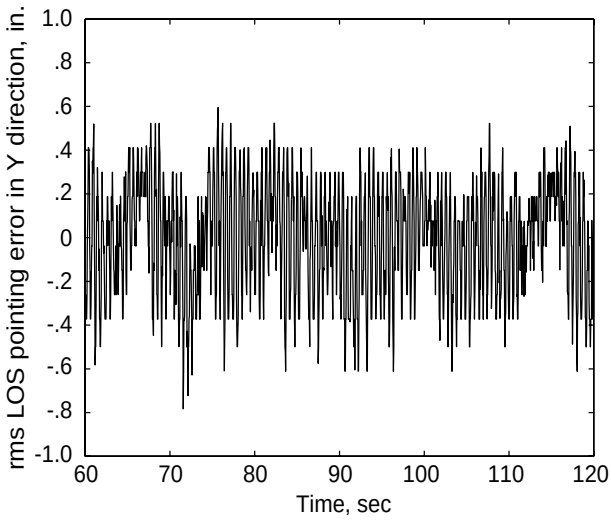

(a) Phase-0 CEM.

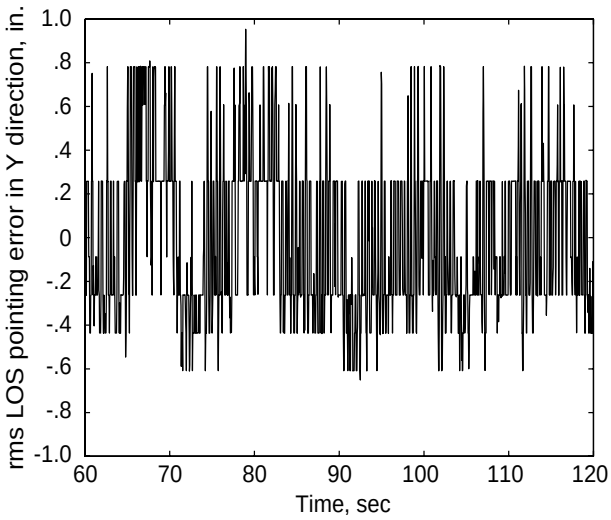

(b) Phase-1 CEM.

Figure 36. LOS pointing error in Y direction with dissipative LQG controller.

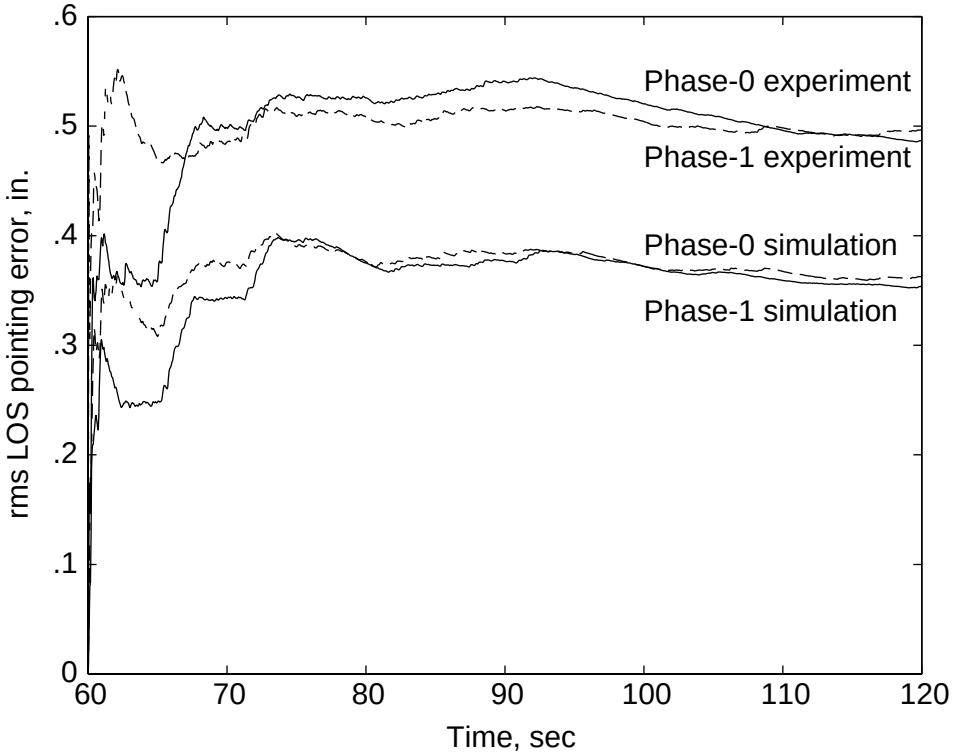

Figure 37. Comparison of rms LOS pointing error with LQG dissipative controllers.

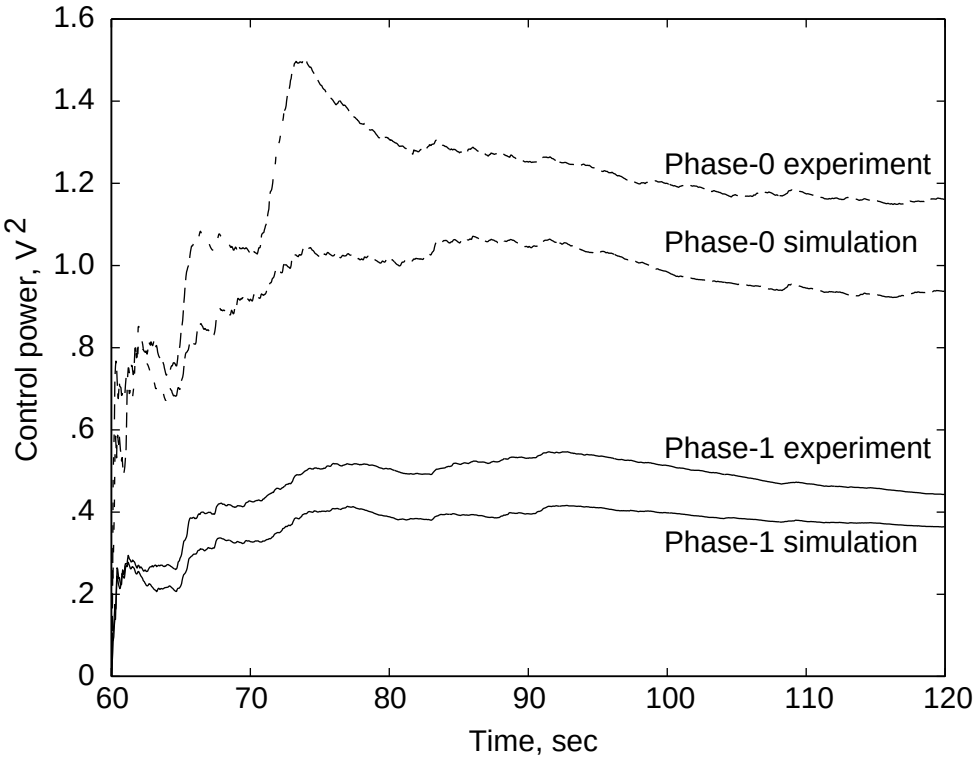

Figure 38. Comparison of average control power with LQG dissipative controllers.

REPORT DOCUMENTATION PAGE

Form Approved
OMB No. 0704-0188

Public reporting burden for this collection of information is estimated to average 1 hour per response, including the time for reviewing instructions, searching existing data sources, gathering and maintaining the data needed, and completing and reviewing the collection of information. Send comments regarding this burden estimate or any other aspect of this collection of information, including suggestions for reducing this burden, to Washington Headquarters Services, Directorate for Information Operations and Reports, 1215 Jefferson Davis Highway, Suite 1204, Arlington, VA 22202-4302, and to the Office of Management and Budget, Paperwork Reduction Project (0704-0188), Washington, DC 20503.

1. AGENCY USE ONLY *(Leave blank)*

2. REPORT DATE
November 1994

3. REPORT TYPE AND DATES COVERED
Technical Paper

4. TITLE AND SUBTITLE
Experimental Validation of an Integrated Controls-Structures Design Methodology for a Class of Flexible Space Structures

5. FUNDING NUMBERS
WU 233-01-01-05

6. AUTHOR(S)
Peiman G. Maghami, Sandeep Gupta, Kenny B. Elliott, Suresh M. Joshi, and Joseph E. Walz

7. PERFORMING ORGANIZATION NAME(S) AND ADDRESS(ES)
NASA Langley Research Center
Hampton, VA 23681-0001

8. PERFORMING ORGANIZATION REPORT NUMBER
L-17358

9. SPONSORING/MONITORING AGENCY NAME(S) AND ADDRESS(ES)
National Aeronautics and Space Administration
Washington, DC 20546-0001

10. SPONSORING/MONITORING AGENCY REPORT NUMBER
NASA TP-3462

11. SUPPLEMENTARY NOTES
Maghami, Elliott, Joshi, and Walz: Langley Research Center, Hampton, VA; Gupta: ViGYAN, Inc., Hampton, VA.

12a. DISTRIBUTION/AVAILABILITY STATEMENT
Unclassified–Unlimited

Subject Category 18

12b. DISTRIBUTION CODE

13. ABSTRACT *(Maximum 200 words)*
This paper describes the first experimental validation of an optimization-based integrated controls-structures design methodology for a class of flexible space structures. The Controls-Structures-Interaction (CSI) Evolutionary Model, a laboratory testbed at Langley, is redesigned based on the integrated design methodology with two different dissipative control strategies. The redesigned structure is fabricated, assembled in the laboratory, and experimentally compared with the original test structure. Design guides are proposed and used in the integrated design process to ensure that the resulting structure can be fabricated. Experimental results indicate that the integrated design requires >60 percent less average control power (by thruster actuators) than the conventional control-optimized design while maintaining the required line-of-sight performance, thereby confirming the analytical findings about the superiority of the integrated design methodology. Amenability of the integrated design structure to other control strategies is considered and evaluated analytically and experimentally. This work also demonstrates the capabilities of the Langley-developed design tool CSI-DESIGN, which provides a unified environment for structural and control design.

14. SUBJECT TERMS
Experimental validation; Integrated controls-structures design; Optimization; Robust control designs

15. NUMBER OF PAGES
43

16. PRICE CODE
A03

17. SECURITY CLASSIFICATION OF REPORT
Unclassified

18. SECURITY CLASSIFICATION OF THIS PAGE
Unclassified

19. SECURITY CLASSIFICATION OF ABSTRACT
Unclassified

20. LIMITATION OF ABSTRACT